BIOHYBRID SWIMMERS AT LOW REYNOLDS NUMBER POWERED BY TISSUE-ENGINEERED NEUROMUSCULAR UNITS

BY

ONUR AYDIN

DISSERTATION

Submitted in partial fulfillment of the requirements
for the degree of Doctor of Philosophy in Mechanical Engineering
in the Graduate College of the
University of Illinois Urbana-Champaign, 2021

Urbana, Illinois

Doctoral Committee:

Professor M. Taher A. Saif, Chair and Director of Research
Professor Rashid Bashir
Assistant Professor Mattia Gazzola
Professor Hyunjoon Kong
Professor Justin S. Rhodes

ABSTRACT

Biohybrid machines are engineered systems which are built by integrating biological cells with synthetic materials and components. Development of biohybrid machines utilizes the classical engineering modalities of design, modeling, prototype fabrication, testing, and iteration, but also draws from a toolbox that includes biological cells and materials. This enables a range of exciting possibilities since biological systems can develop via self-organization, function autonomously, and monitor and adapt to their environments. Pioneering studies on biohybrid machines have demonstrated the development of devices powered by muscle cells, capable of locomotion, pumping, and micromanipulation. A currently emerging frontier in the field is the integration of neuronal control. A wide range of complex animal behaviors are orchestrated by the nervous system which interfaces the body with the environment through sensing, information processing, and coordinating motor activity. Hence, the integration of neurons may enable the development of autonomous biohybrid machines capable of higher-level functionalities such as sensing, memory, and adaptation.

The focus of this dissertation is on the implementation of neuronal actuation in muscle powered biohybrid machines. Firstly, we develop an experimental bioactuator platform to study the *in vitro* development of neuromuscular units. Engineered skeletal muscle tissues, anchored to compliant pillars, are co-cultured on the platform with optogenetic stem cell-derived neuronal clusters containing motor neurons. The motor neurons extend axons and innervate the muscle fibers, forming functional neuromuscular units. Our study illustrates several outcomes of synergistic interactions between the muscles and neurons. Muscles co-cultured with neurons exhibit significantly higher contraction force and cytoskeletal maturation compared to muscles cultured alone. Neurons self-organize into networks which generate synchronous bursting patterns, the development of which is facilitated by muscle-secreted soluble factors.

Next, we implement our neuron-muscle co-culture approach on a free-standing compliant scaffold containing slender flagella, to demonstrate the first example of a biohybrid swimmer powered by neuromuscular units. Optogenetic stimulation of motor neurons evokes periodic muscle contractions, and the swimmer is driven by the resulting time-irreversible deformations of the flagella, a common mechanism of propulsion at low Reynolds number. Lastly, we investigate

potential design strategies for improving swimming performance, assisted by analytical and computational models. Our models predict that the swimming speed of our initial prototype can be improved by up to two orders of magnitude by redesigning the swimmer scaffold to reduce drag and increase actuation amplitude.

ACKNOWLEDGMENTS

I am grateful to my parents Ahmet and Nuket Aydin and my sister Cansu, for their support and encouragement throughout my entire education. I would not be where I am now without them.

I thank my PhD advisor, Professor Taher Saif, for his excellent mentorship. His guidance has been invaluable in my pursuit of an academic career. His passion for scientific inquiry and his commitment to teaching and mentoring is a source of inspiration. I would also like to thank my thesis committee members, Professors Rashid Bashir, Mattia Gazzola, Hyunjoon Kong, and Justin Rhodes, for their guidance and feedback.

I would like to thank my lab mates Dr. Brian Williams, Dr. Samantha Knoll, Iris Choi, Dr. Mohamed Elhebeary, Dr. Anthony Fan, Dr. Zhengwei Li, Bashar Emon, Umnia Doha, Saddam Hussein Joy, Ki Yun Lee, and William Drennan, for their support and feedback.

Throughout my PhD, I have had the pleasure and privilege of working with many outstanding researchers from numerous disciplines. I appreciate all the help they have graciously offered, whether through direct involvement in research activities, by providing training and access to laboratories, or through insightful discussions and feedback. I would like to express my gratitude to: Professor Rashid Bashir and his lab members Dr. Gelson Pagan-Diaz, Dr. Caroline Cvetkovic, Dr. Ritu Raman, Jiaojiao Wang, and Yongdeok Kim; Professor Mattia Gazzola and his students Xiaotian Zhang and Andrew Dou; Professor Steven Stice and his lab members Dr. Austin Passaro and Dr. Raymond Swetenburg; Professor Justin Rhodes and his student Jennie Gardner; Professor Marni Boppart and her student Dr. Svyatoslav Dvoretskiy; Professor Hyunjoon Kong and his lab members Dr. Eunkyung Ko, Dr. Ellen Qin, and Dr. Yongbeom Seo; Professor Roger Kamm and his students Dr. Sebastien Uzel and Dr. Tatsuya Osaki; Professor Gabriel Popescu and his student Dr. Mikhail Kandel; Professor Martha Gillette, her group's research scientist Dr. Jennifer Mitchell, and her students Dr. Collin Kaufman and Dr. Chris Liu; Professor Rhanor Gillette; Professor John Rogers; Professor Glennys Mensing and Joe Maduzia at the Micro-Nano-Mechanical Systems Cleanroom; and Dr. Mayandi Sivaguru, Dr. Austin Cyphersmith, and Dr. Kingsley Boateng at the Institute for Genomic Biology at University of Illinois at Urbana-Champaign.

I have had the distinct pleasure of mentoring undergraduate students Sittinon Nuethong, Chris Chen, Kenta Hirashima, Roy Brooks Rivera, Victor Ariyo, and Michael Chi, on various research projects in our lab. I hope that my mentorship has been satisfactory and that they have enjoyed their research experience.

The work presented in this dissertation was funded by the National Science Foundation through Science and Technology Center for Emergent Behaviors of Integrated Cellular Systems (Grant 0939511), and Emerging Frontiers in Research and Innovation: Continuum, Compliant, and Configurable Soft Robotics Engineering (Grant 1830881).

TABLE OF CONTENTS

CHAPTER 1: INTRODUCTION

1.1 Background: muscle powered biohybrid machines

A major focus during the first few decades of modern bioengineering has been on fabricating multicellular constructs which mimic the form and function of existing biological systems, essentially reverse engineering tissues and organs for medical applications. More recent advances, however, have expanded the field's focus to include forward engineering of multicellular systems with capabilities beyond those observed in nature [1]. This enables exciting possibilities, as biologically powered systems can autonomously process and modulate a wide range of environments with higher efficiency and efficacy compared to purely abiotic systems. Forward engineering of biological systems that effectively leverage the emergent behaviors predominant in biology requires developing a better understanding of biological building blocks and how they interact with one another in complex environments. At the same time, the construction of novel biological and biohybrid systems may shed new light onto the design principles underlying biology [2].

Among the novel engineered multicellular systems are biohybrid machines which are built by integrating biological cells and artificial structures [3], [4]. Research during the earlier decades of bioengineering has produced a body of knowledge on how muscle cells embedded within engineered microenvironments can form contractile units; what roles cell-cell and cell-matrix interactions play; and how the morphology, physiology, and mechanical performance of the engineered muscle constructs depend on various experimental factors [5]–[8]. Consequently, there has been a proliferation of studies in recent years demonstrating the development of muscle-based bioactuators [9]–[12] and their implementation in biohybrid soft robotic devices capable of micromanipulation [13], pumping [14], [15], and untethered locomotion via swimming [16]–[19] and walking [19]–[22].

These pioneering studies have set the foundation for the design and fabrication of muscle powered biohybrid machines. They have also demonstrated some of the notable abilities of biological muscle including distributed and sequential actuation through gap junction mediated cell-cell connectivity [18], adaptive strengthening through exercise [23], self-healing of muscle tissue after mechanical damage [24], and modulation of enzymatic degradation and bioactuator lifetime [25].

1.2 Aims and scope: neuromuscular actuation

The aim of this dissertation is to achieve neuronal control of muscle powered actuation in biohybrid machines, using a low Reynolds number biohybrid swimmer as a test case. A wide range of complex animal behaviors rely on the nervous system which interfaces the body and the environment through sensing, information processing, and coordinating motor activity [26]. Hence, the integration of neuronal actuation with biohybrid machines may launch a new frontier in the field of bioengineering, leading to the development of future biohybrid machines with engineered nervous systems capable of autonomous navigation, sensing, memory, and adaptation.

In vertebrate animals, motor activity is orchestrated by the neural circuits of the spinal cord and the brain [27]–[29]. These circuits interface with muscles through motor neurons. A motor neuron and the muscle fibers that it innervates constitute a neuromuscular unit, where the communication is mediated via synapses called neuromuscular junctions (NMJs) [27]. *In vitro* development of neuromuscular units with functional NMJs is, therefore, the first key milestone towards achieving neuronal control of muscle powered biohybrid machines.

The NMJ has been studied extensively since mid-20th century, leading to a substantial amount of literature on the development, function, physiology, anatomy, and pharmacology of the synapse. In fact, studies of the NMJ predate those of neuron-neuron synapses, and have contributed to most of our understanding of synaptic transmission in general. This is because the NMJ is simpler and more easily accessible for experimental observation and manipulation compared to synapses between neurons within the central nervous system [26]. Most of the earlier studies consisted of *in vivo* observations and *in vitro* experiments with co-cultures of muscle tissue and spinal cord explants or of primary muscle cells and motor neurons [30]–[32]. In addition to elucidating the physiology and anatomy of the synapse, the earlier studies of NMJs have also revealed a key insight: The neuromuscular unit is a complex biological system which emerges through synergistic interactions between muscle cells and neurons. One of the hallmarks of NMJ development is the high degree of reciprocal inductive interactions between neurons and muscles. These interactions involve spontaneous activity and soluble factor-mediated signaling, and play key roles in attaining neuromuscular units with proper form and function [33]–[36].

However, despite the extensive body of knowledge and insights on the biology of the NMJ, building neuromuscular bioactuators remains a significant challenge. While classical biological sciences aim to decipher how existing biological systems develop and function in nature,

engineering biohybrid machines requires an understanding of how the system can be developed *de novo* from the essential building blocks (*e.g.*, cells, extracellular matrix, and synthetic scaffolds) to attain the desired form and function.

To build a neuromuscular biohybrid swimmer capable of untethered locomotion, neuromuscular units must be developed on a free-standing compliant scaffold where the evoked muscle contractions generate the body deformations necessary for swimming. The vast majority of *in vitro* NMJ studies have been performed by establishing neuron-muscle co-cultures on 2D and rigid substrates. Free-standing and 3D tissue engineered neuromuscular units have been demonstrated only by a handful of studies published in recent years [37]–[41], most of which were performed concurrently with the work presented in this dissertation. Designing and building experimental test platforms for the *in vitro* development of neuromuscular bioactuators is therefore the necessary first step to achieve the aim of this dissertation.

1.3 Organization of the dissertation

We begin by addressing the challenge of building neuromuscular bioactuators to power biohybrid machines. Chapter 2 presents our work on developing free-standing neuron-muscle co-culture on a 3D and compliant platform [42], to serve as a test-bed for subsequent bioactuator designs. Using this platform, in conjunction with microelectrode arrays (MEA), we study the roles of synergistic interactions between neurons and muscles on the co-development of muscle tissues and neural networks. Next, we implement our methodology for neuromuscular bioactuator development on a modified scaffold design to build a biohybrid swimmer operating at low Reynolds number. Chapter 3 presents our first neuromuscular swimmer prototype [43], where we focus on the development and function of the neuromuscular bioactuator. In Chapter 4, we shift our focus to the swimming performance, and investigate potential design strategies to improve swimming speed by up to two orders of magnitude. To predict swimming speed, we develop analytical models that account for the hydrodynamic forces, scaffold elasticity, and muscle contraction dynamics. Guided by our model predictions, we design novel scaffolds and develop appropriate tissue culture techniques to help build swimmers with improved performance. Lastly, in Chapter 5, we summarize the current state of the art and discuss future challenges including the development of neuronal circuitry for higher-level functions such as sensing, motor coordination, memory, and learning, as well as the real-world applications of biohybrid machines.

CHAPTER 2: IN VITRO DEVELOPMEMT OF NEUROMUSCULAR BIOACTUATORS

This chapter is adapted from a previous publication[*].

2.1 Multi-target 3D neuron-muscle co-culture platform

Here, we demonstrate a microfabricated polydimethylsiloxane (PDMS) platform for multi-target neuron-muscle co-culture in a 3D and compartmentalized setting. The platform has a central compartment to host a neurosphere surrounded by four target compartments each containing a pair of compliant T-shaped pillars to anchor the target tissues and measure contraction forces (Fig. 2.1A). All compartments have a nominal depth of 200 μm, enabling 3D culture settings while still allowing visualization of tissues under a light microscope. Neuron-muscle co-culture is achieved in two stages (Fig. 2.1B): First, the target muscle tissues are formed by mixing skeletal myoblasts with an extracellular matrix (ECM) solution consisting of type I collagen and Matrigel, and seeding the mixture directly into the target wells by pipette. The ECM solution polymerizes, forming a cell-laden hydrogel, which is then compacted by the traction forces of the myoblasts. This process results in free-standing muscle tissues anchored to the tips of the two compliant pillars (Fig. 2.1C). This configuration also allows quantification of muscle contraction forces by optically measuring pillar deflections. In the second stage, co-culture is initiated by seeding a stem cell-derived neurosphere containing motor neurons (MNs) in the central compartment, then filling the entire platform with fresh ECM (Fig. 2.1D). The addition of new ECM provides a continuous hydrogel embedding both the target tissues and the neurosphere, through which neurons can extend axons towards their targets.

This platform serves as a useful testbed for the development of neuromuscular bioactuators for untethered biohybrid machines since the co-culture is established in the form of a free-standing tissue, and the muscle tissues are anchored to compliant structures which allow quantification of the displacements and forces generated by evoked contractions.

[*] [42] O. Aydin *et al.*, "Development of 3D neuromuscular bioactuators," *APL Bioeng.*, vol. 4, no. 1, 2020.

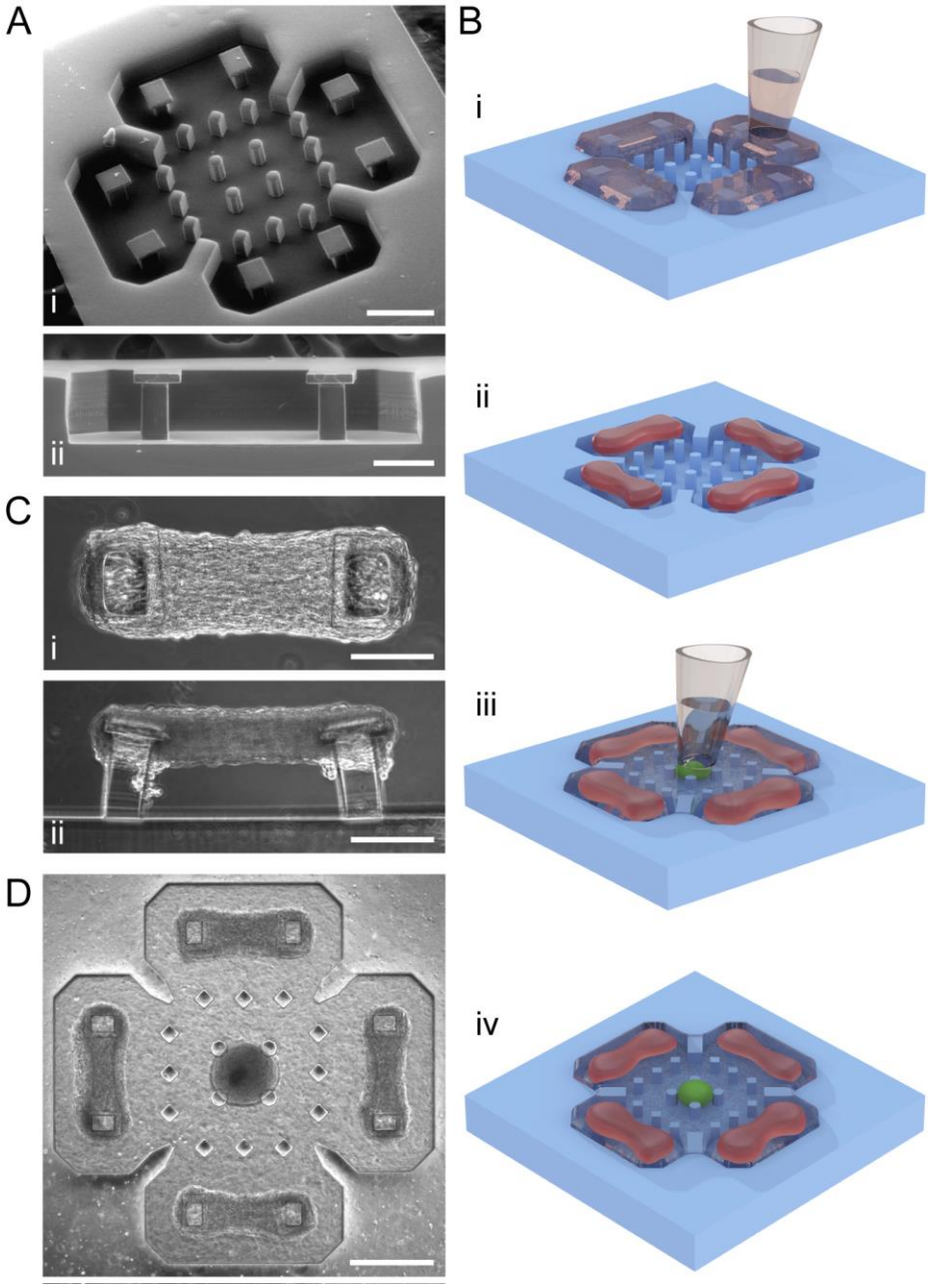

Figure 2.1: 3D neuron-muscle co-culture in a bioactuator platform. (A) SEM images of (i) the full platform and (ii) one of the target wells showing the pillar profile. (B) Schematic of tissue seeding process illustrating (i) target cell-ECM seeding, (ii) compacted target tissues, (iii) neurosphere seeding, (iv) and co-culture tissue. (C) Phase contrast images of a muscle strip from (i) top and (ii) side views. (D) Phase contrast image of the full platform after neurosphere seeding. Scale bars: (A-i and D) 500 µm, (A-ii, C-i, and C-ii) 200 µm.

The simple approach of seeding tissues directly by pipetting makes it possible to design a multi-target platform which improves experimental yield by increasing number of target tissues per neuronal cluster. This multi-target architecture may also allow our platform serve as a useful testbed for modeling bioactuators that employ multiple muscle tissues such as the system recently demonstrated by Morimoto *et al.* which involved a pair of antagonistic muscles on a compliant scaffold [44]. Furthermore, the present platform design provides about 500 µm separation between the neurosphere and target tissues (Fig. 2.1D), thus allowing the use of the platform to investigate long-range interactions. This compartmentalization is enabled by the hydrophobicity of PDMS: In each target well, the side that faces the central compartment has three posts separated by small (120 µm) gaps. When the liquid cell-ECM mixture is seeded only into the target wells, hydrophobicity of PDMS induces formation of menisci between the posts [45], preventing the liquid cell-ECM mixture from leaking into the central compartment (Fig. 2.2A-B). Once the ECM solution gels, the platform is inundated with culture media, resulting in intact cell-laden ECM gels confined to the target wells (Fig. 2.2C).

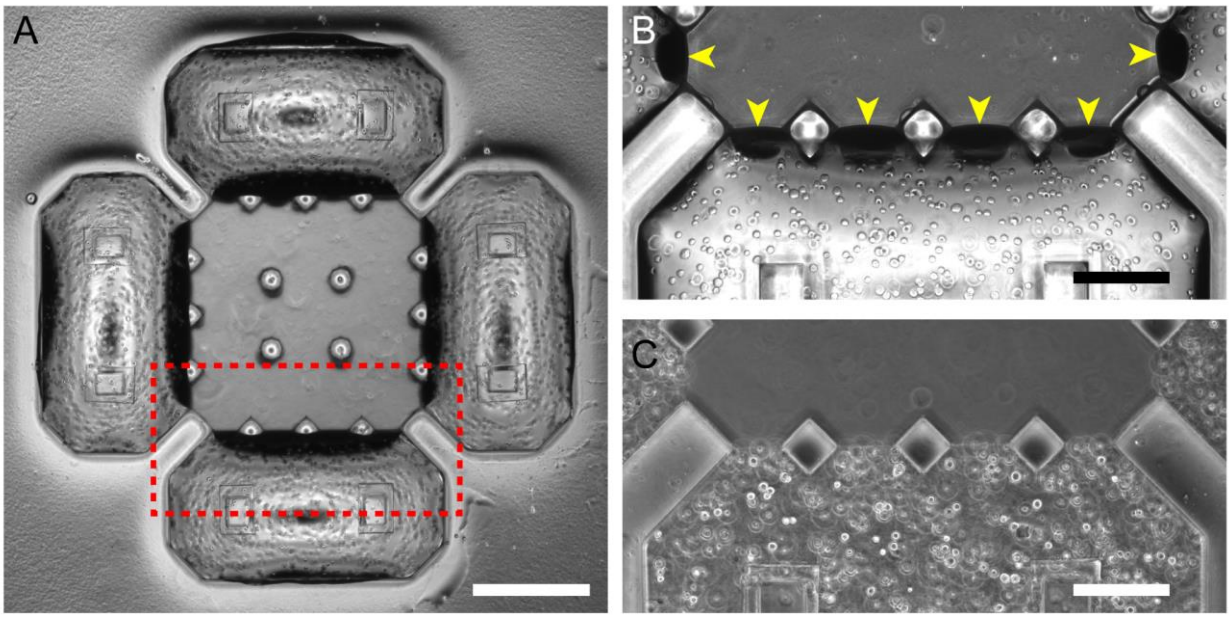

Figure 2.2: Compartmentalized cell seeding. (A) Phase contrast image of a full platform immediately after seeding myoblast-ECM mixture into the target wells. Scale bar: 500 µm. (B) Close up view of the region outlined by dashed lines in A. Arrows point to the menisci. Scale bar: 200 µm. (C) Phase contrast image of the same region immediately after inundation with culture medium, illustrating the intact cell-laden ECM gel confined to the target well. Scale bar: 200 µm.

2.2 Characterization of neuromuscular bioactuators

We developed co-cultures in our platform using C2C12 mouse skeletal myoblasts to create target muscle strips and co-culturing them with neurospheres that were obtained by directed differentiation of an optogenetic mESC line towards motor neurons (see Section 2.6 Materials and methods). After initiating co-culture, we observed neuronal outgrowth during the first 2-3 days. We then monitored co-cultures and performed optical stimulation to assess the formation of NMJs. In all optical stimulation assays, the entire field of view was illuminated with blue light for 1 second while continuously recording video of the sample to capture muscle activity before, during, and after stimulation. To confirm that illuminating the entire sample does not lead to unintended stimulation of muscle strips, we prepared muscle-only control samples where muscle strips were formed and embedded in 3D ECM gel without a neurosphere. Muscle activity was quantified in terms of the contraction force produced by the muscle strips.

We began to observe muscle contractions in response to optical stimulation of MNs around day 4-5 of co-culture, corresponding to about 2 days after neurites reach the target muscle strips. In terms of NMJ formation timeline, this is in agreement with previously reported results using the same cell sources [38]. Interestingly, in addition to contractions evoked by stimulation of MNs, some muscle strips also developed rhythmic spontaneous contraction patterns that were present before neuronal stimulation. By day 7, we identified three different muscle behaviors in response to optical stimulation of neurons (Fig. 2.3A): no change in contraction pattern (21/88 muscle strips), evoked contractions in muscles that were quiescent before stimulation (19/88 muscle strips), and evoked as well as spontaneous contractions (48/88 muscle strips). The presence of evoked muscle contractions in the latter two groups suggest the formation of functional NMJs, and these groups comprised 76% of the muscle strips. For further analysis, we refer to muscles that are quiescent before stimulation as group 1 and muscles spontaneously contracting before stimulation as group 2 (Fig. 2.3B).

To quantify the effect of optical stimulation, we analyzed the muscle contraction dynamics. For each muscle strip, we computed the contraction force and frequency averaged over the 10 contractions immediately before and the 10 immediately after stimulation. Here, we define the contraction frequency as $1/\tau$ where τ is the contraction period measured as the time between two consecutive contractions (Fig. 2.3C). In group 1 the effect of neuronal stimulation is self-evident since muscle strips are quiescent before stimulation and produce contractions with 39.0±34.4 μN

(mean ±SD) force upon neuronal stimulation (Fig. 2.3D). In group 2, there was no significant difference in contraction force before and after stimulation. There was also no significant difference in strength of evoked contractions in groups 1 and 2 (Fig. 2.3E). However, the evoked contractions in group 2 can be quantitatively distinguished from spontaneous contractions by their significantly higher frequency (Fig. 2.3F). In addition, we observed no effect of light on the contraction dynamics in muscle-only control samples, indicating that contractions evoked by optical stimulation in co-culture samples are due to the formation of NMJs between muscle strips and MNs.

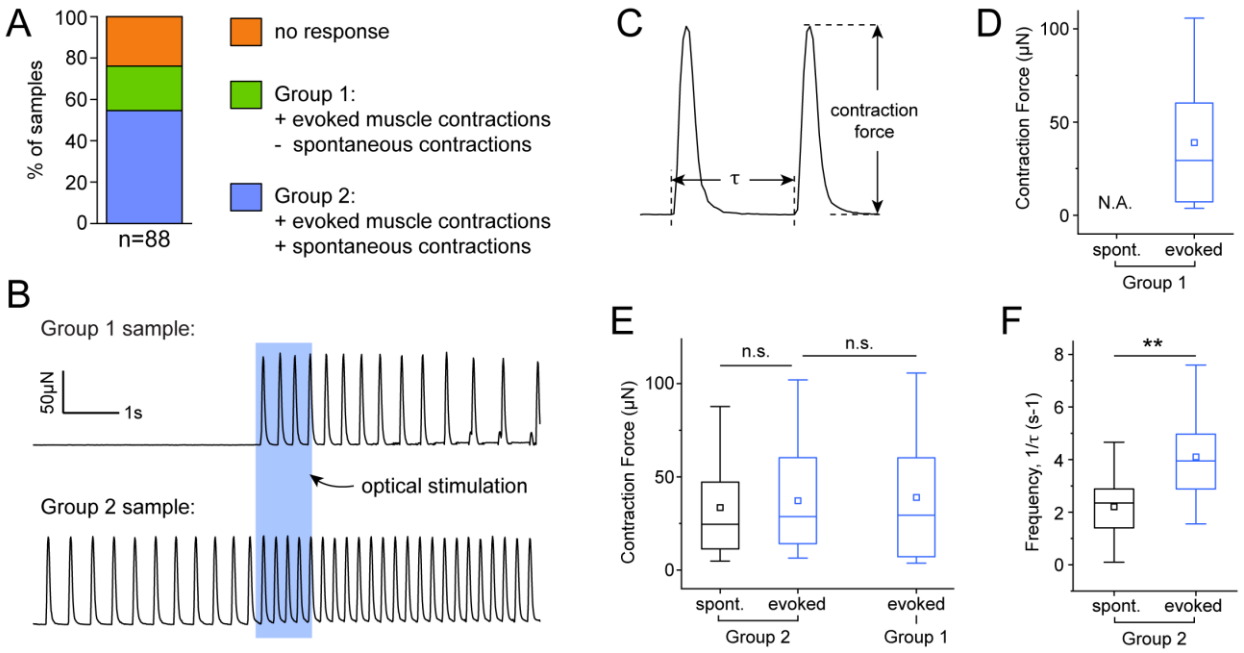

Figure 2.3: Formation of functional neuromuscular junctions. (A) Muscle strips categorized by their contraction pattern in response to optical stimulation of neurons. (B) Force-time traces of representative samples from groups 1 and 2. Blue rectangle indicates optical stimulation. (C) Definitions of contraction force and period. (D-E) Comparison of spontaneous and evoked contraction forces in groups 1 and 2. (F) Comparison of spontaneous and evoked contraction frequencies in group 2. Values in panels D, E, and F are averaged over the 10 contractions immediately preceding and following optical stimulation for spontaneous and evoked contractions, respectively. Box plots represent 25th, 50th, and 75th percentiles with whiskers representing 1.5x inter-quartile range, n=19 muscle strips for group 1 and n=48 muscle strips for group 2, **p<0.005 (Student's t-test).

Furthermore, we performed immunofluorescence assay to confirm the morphology of neuromuscular units. The C2C12 myoblasts embedded in 3D ECM had differentiated to form multinucleated muscle fibers with cross-striations (Fig. 2.4A-C), and neurites extended towards the fibers and made physical connections with post-synaptic acetylcholine receptor clusters (Fig. 2.4D-F). Taken together, these results illustrate the formation of optically excitable functional NMJs between MNs in stem cell-derived neurospheres and engineered skeletal muscle tissue constructs in our co-culture platform.

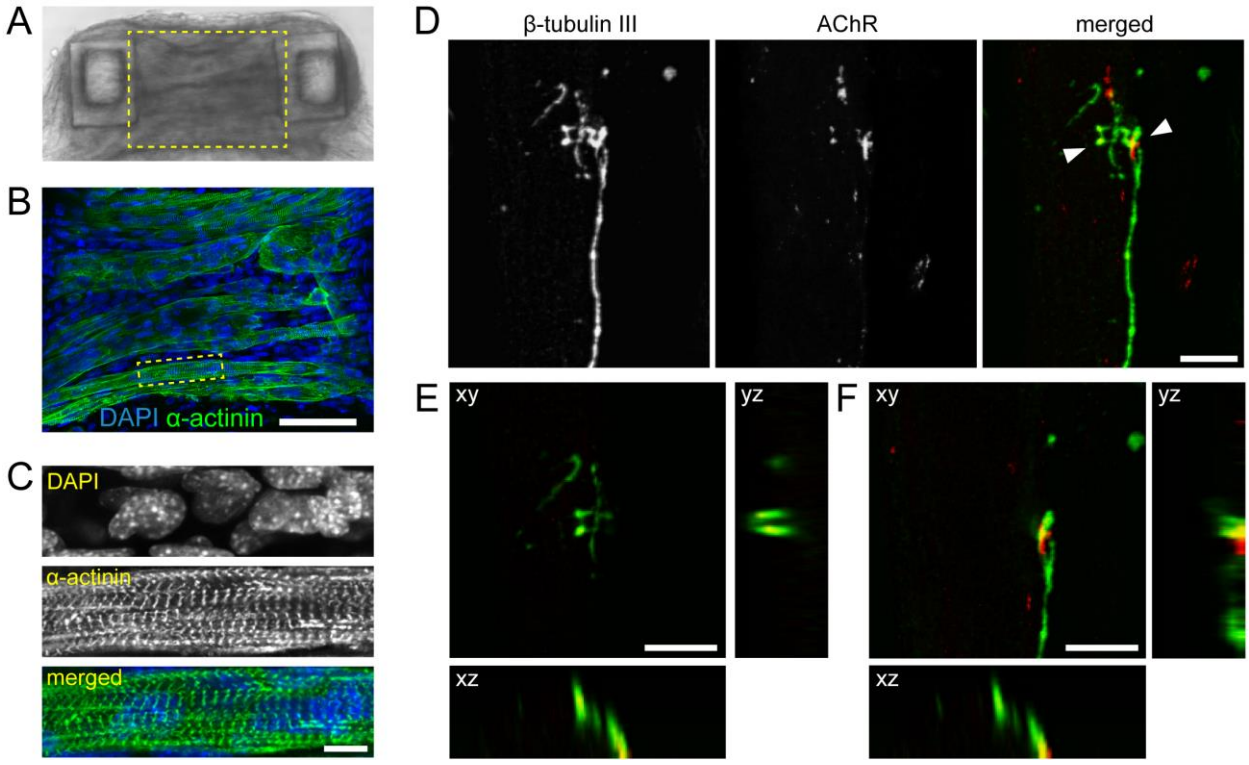

Figure 2.4: Morphological characterization of muscle tissues and NMJs. (A) Brightfield image of a muscle strip and (B) confocal image of the region outlined in A, showing the muscle fibers within the tissue. (C) Zoomed-in views of the region outlined in B, showing a muscle fiber with cross-striations. (D) Confocal images illustrating a neurite (β-tubulin III, green) extending towards and making connections with post-synaptic receptor clusters on the muscle membrane (AChR, red). (E-F) Orthogonal views of the regions indicated by the arrowheads in the rightmost panel in D. Scale bars: (B) 100 μm, (C-F) 10 μm.

2.3 Neuronal outgrowth towards different targets

During the formation of neuromuscular units discussed above, we observed neuronal outgrowth towards the muscle tissues during the first 2-3 days of co-culture. There has been experimental evidence suggesting that soluble factors secreted by muscles promote neuronal outgrowth from MNs in both isolated cultures [46] and co-cultures [47]. To investigate if such an effect is present in our co-culture platform, we capitalized on the multi-target and compartmentalized design of the platform and cultured neurospheres with different targets. We performed two sets of experiments where the targets were muscle tissues and acellular ECM in case 1 (Fig. 2.5A), and muscle tissues and fibroblast tissues in case 2 (Fig. 2.5B). We allowed the co-cultures 3 days and then took fluorescent microscopy images of Hb9-GFP$^+$ MNs to visualize outgrowth. To compare outgrowth towards different targets, we draw an annulus centered around the neurosphere, divide it into four sectors corresponding to the regions between the neurosphere and each target, and for each sector quantify the ratio of total fluorescent light intensity in that sector to the total intensity in the entire annulus as a measure of the relative degree of outgrowth towards that target (Fig. 2.5C-i).

In case 1, we observed significantly more outgrowth towards muscle tissues compared to acellular ECM. While this result does support the idea that the presence of muscles can enhance neuronal outgrowth, the mechanism of interaction is ambiguous in this case: As engineered tissue constructs form, due to compaction and remodeling of the ECM, their rigidity increases from initial levels comparable to that of acellular ECM to as much as an order of magnitude higher values [48]. This can lead to muscle strips and acellular ECM providing different mechanical cues and therefore makes it difficult to ascertain whether the biased outgrowth is due to mechanical or biochemical signals. To resolve this issue, we performed the experiments in case 2 where the alternate targets were fibroblast tissues. Fibroblasts embedded in ECM generate compaction and remodeling of the ECM [49] same as muscles, thus eliminating the asymmetry in mechanical cues. Analysis of the case 2 samples also revealed biased outgrowth towards muscles (Fig. 2.5C-ii), suggesting that neuronal outgrowth towards muscles may indeed be enhanced due to muscle-specific soluble factors.

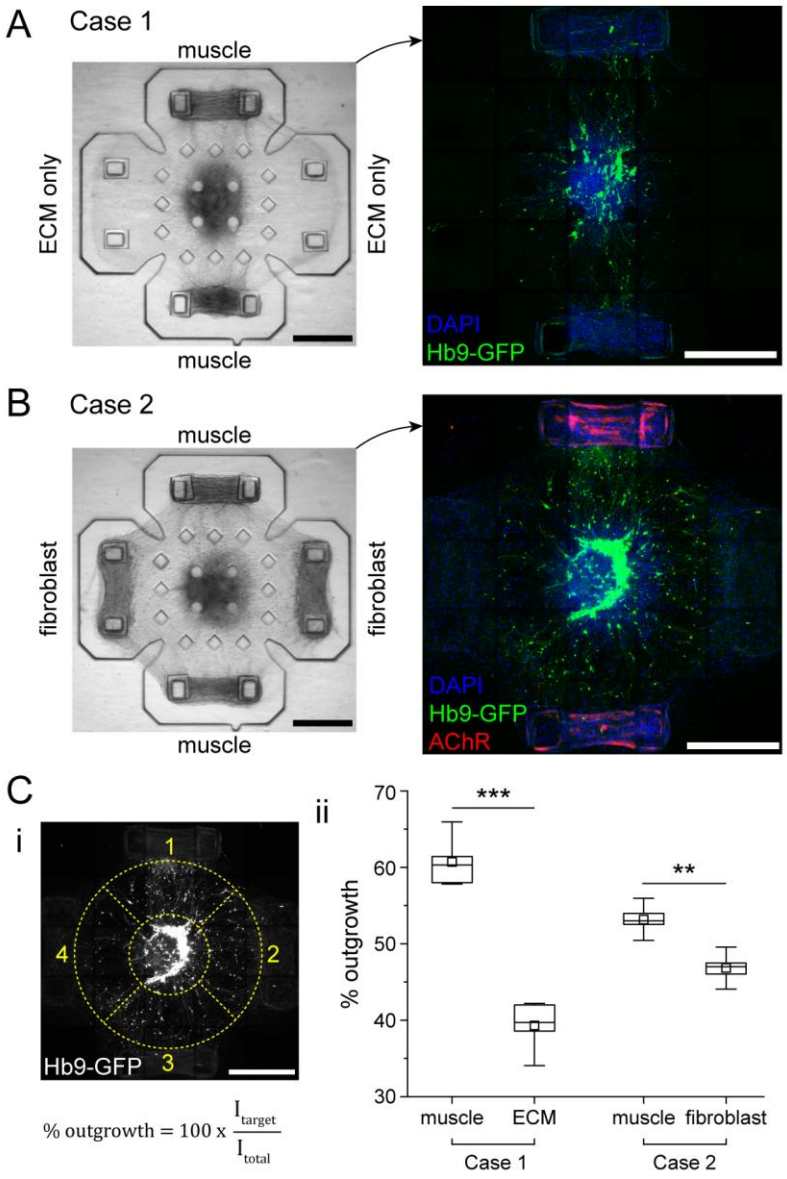

Figure 2.5: Neuronal outgrowth towards different targets. (A-B) Brightfield and corresponding confocal images of representative samples from (A) case 1 and (B) case 2. (C) (i) Confocal image of motor neurons with the outlines in dashed lines illustrating the four different sectors that correspond to the regions between the neurosphere and the different targets, and the definition of % outgrowth where 'I' refers to the total fluorescent light intensity. (ii) Comparison of relative outgrowth towards the different targets in cases 1 and 2. Values are % outgrowth towards each type of target, box plots represent 25th, 50th, and 75th percentiles with whiskers representing 1.5x inter-quartile range, n=5 co-culture samples each for cases 1 and 2, **p<0.005 and **p<0.0005 (Student's t-test). All scale bars: 500 µm.

2.4 Co-development of muscle tissues and neural networks via synergistic interactions

During the development of neuromuscular units in our platform, we observed an emergence of spontaneous contraction patterns in most of the samples. Developing skeletal muscle fibers can exhibit spontaneous action potentials and corresponding contractions even in the absence of neurons [50] possibly due to self-activation of acetylcholine receptors (AChRs) by endogenous secretion of acetylcholine (ACh) [51]. However, the abundance of spontaneous contractions in our co-cultures prompted us to ask whether they may also be neural induced. To investigate, we monitored the spontaneous contractions of muscle strips cultured alone and those co-cultured with neurospheres in our platform. Activity of muscles from both groups were recorded at days 3, 5, and 7 without external stimulation. In co-cultures, the relative number of muscle strips that exhibited spontaneous contractions (*i.e.*, active muscle strips) began to increase at day 5, reaching 67% at day 7 (Fig. 2.6A-i) whereas in the muscle only group, the relative number of active muscle strips remained below 30% (Fig. 2.6A-ii).

In addition to overall contractile activity, we measured and compared the force magnitude of spontaneous contractions (Fig. 2.6B). At day 3, muscles in both groups were either quiescent or had relatively weak spontaneous contractions with no significant difference in magnitude between muscle-only and co-culture samples. However, starting at day 5, the co-cultured muscle strips had significantly higher spontaneous contraction force compared to muscle-only group. By day 7, spontaneous contraction forces as high as 102 μN were recorded in co-culture whereas the maximum spontaneous contraction force in muscle-only group was 18.8 μN (Fig. 2.6B). Given this significantly higher spontaneous contraction force in co-cultured muscle strips, we performed immunofluorescence staining of sarcomeric α-actinin on muscle strips from both groups at day 7. In each muscle strip, we observed cross-striated muscle fibers as well as fibers without cross-striations. The relative number of cross-striated muscle fibers was significantly higher in co-cultured muscle strips (70±8%, n=6 muscle strips) compared to muscle-only (41±6%, n=6 muscle strips) (Fig. 2.6C), indicating that muscles in co-culture had a relatively higher degree of contractile apparatus assembly. This offers a possible explanation for the measurement of higher spontaneous contraction force in co-cultures.

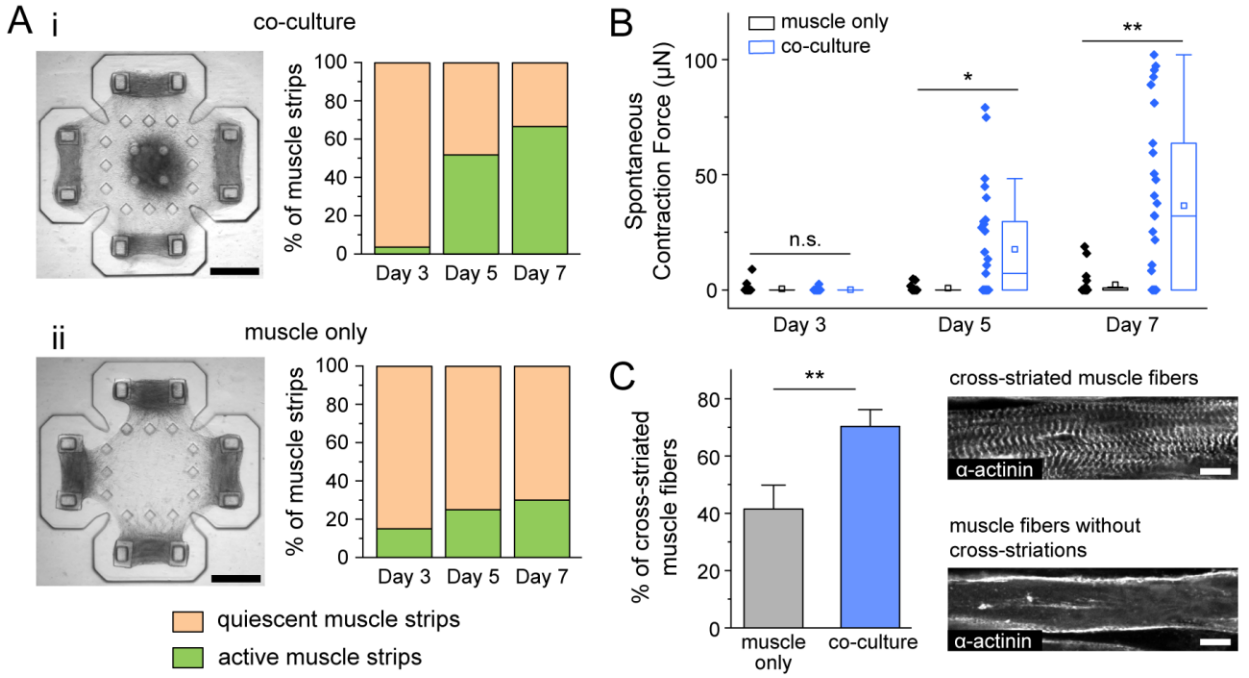

Figure 2.6: Enhanced contractility and sarcomere assembly in muscles co-cultured with neurospheres compared to muscles in monoculture. (A) Representative brightfield images and overall time course of the ratio of active vs quiescent muscle strips in (i) co-cultures and (ii) muscle-only cultures. Scale bars: 500 μm. (B) Spontaneous contraction forces in muscle-only and co-culture samples at days 3, 5, and 7. Values are spontaneous contraction force averaged over a 30 second recording per muscle strip at each day, box plots represent 25th, 50th, and 75th percentiles with whiskers representing 1.5x inter-quartile range, n=27 muscle strips for co-culture and n=20 muscle strips for muscle-only at each day, *p<0.05 and **p<0.005 (Mann Whitney U test). (C) Comparison of the percentage of cross-striated muscle fibers between muscle-only and co-culture groups. Bars represent mean+SD, n=6 muscle strips for each group, **p<0.005 (Mann Whitney U test). Confocal images at the right show sample muscle fibers with and without cross-striations. Scale bars: 10 μm.

These results prompt the question of how co-culture with neurons could induce higher levels of spontaneous muscle contractility. Previous studies on neuromuscular units, both *in vivo* and *in vitro*, have shown that MNs spontaneously secrete ACh during development [52]–[54], that there is a marked increase in spontaneous neural activity shortly after neurons contact muscles [55], and that this activity can induce contractions in the innervated muscle [56]. Furthermore, recent *in vivo* work has demonstrated that spontaneous muscle contractions precede and contribute to sarcomere assembly [57]. Spontaneous firing of neurons and corresponding synaptic transmission is therefore a likely explanation of how the muscles in co-culture in our platform develop more and stronger spontaneous contractions and the associated increase in contractile apparatus assembly. This is further supported by the observation that in our platform, the effect of

NMJ formation (*i.e.*, muscle contractions in response to optical stimulation of MNs) begins to appear around day 4-5 of co-culture and that the significant increase in spontaneous muscle contractility also begins at day 5.

To test if our stem cell-derived neurons can develop spontaneous firing patterns, we used MEA electrophysiology. In MEA recordings from developing neural cultures, the following spontaneous activity pattern can typically be observed: First, cells begin firing randomly, with spikes corresponding to single action potentials observed scattered throughout the MEA. Cells then begin firing in bursts, or trains of spikes. Finally, as neural connectivity increases, the neural networks begin to fire in synchronized bursts [58]–[60]. We dissociated our neurospheres at the last day of neural differentiation (corresponding to day 0 of co-culture in the 3D NMJ platform), plated them on MEAs at high cell density (Fig. 2.7A-C), and recorded electrical activity over time. After 9 days in culture, we observed spiking and bursting activity in a few electrodes, indicating spontaneous neural activity, but the activity level across the entire culture was relatively low as most electrodes were quiescent (Fig. 2.7D). This is not surprising since previous studies have shown that with stem cell-derived neurons, the development of robust bursting activity can take several weeks [61], [62].

However, since spontaneous neural activity during *in vivo* NMJ development increases markedly shortly after neurons contact muscles [55], we postulated that muscle-secreted factors may enhance neural firing. To test this, we cultured neurons on MEAs in muscle-conditioned medium (CM, collected from separate C2C12 cultures) to emulate the postulated soluble factor-mediated retrograde signaling. Strikingly, neurons cultured in muscle CM had substantially improved spontaneous activity, exhibiting periodic and synchronous busts at day 9 (Fig. 2.7E). Quantitatively, the effect of muscle CM corresponded to increased bursting rates with the difference to control group becoming significant starting at day 5 (Fig. 2.7F). In terms of timeline, this matches closely with the increase in muscle contractility that we observed in co-cultures starting around day 5.

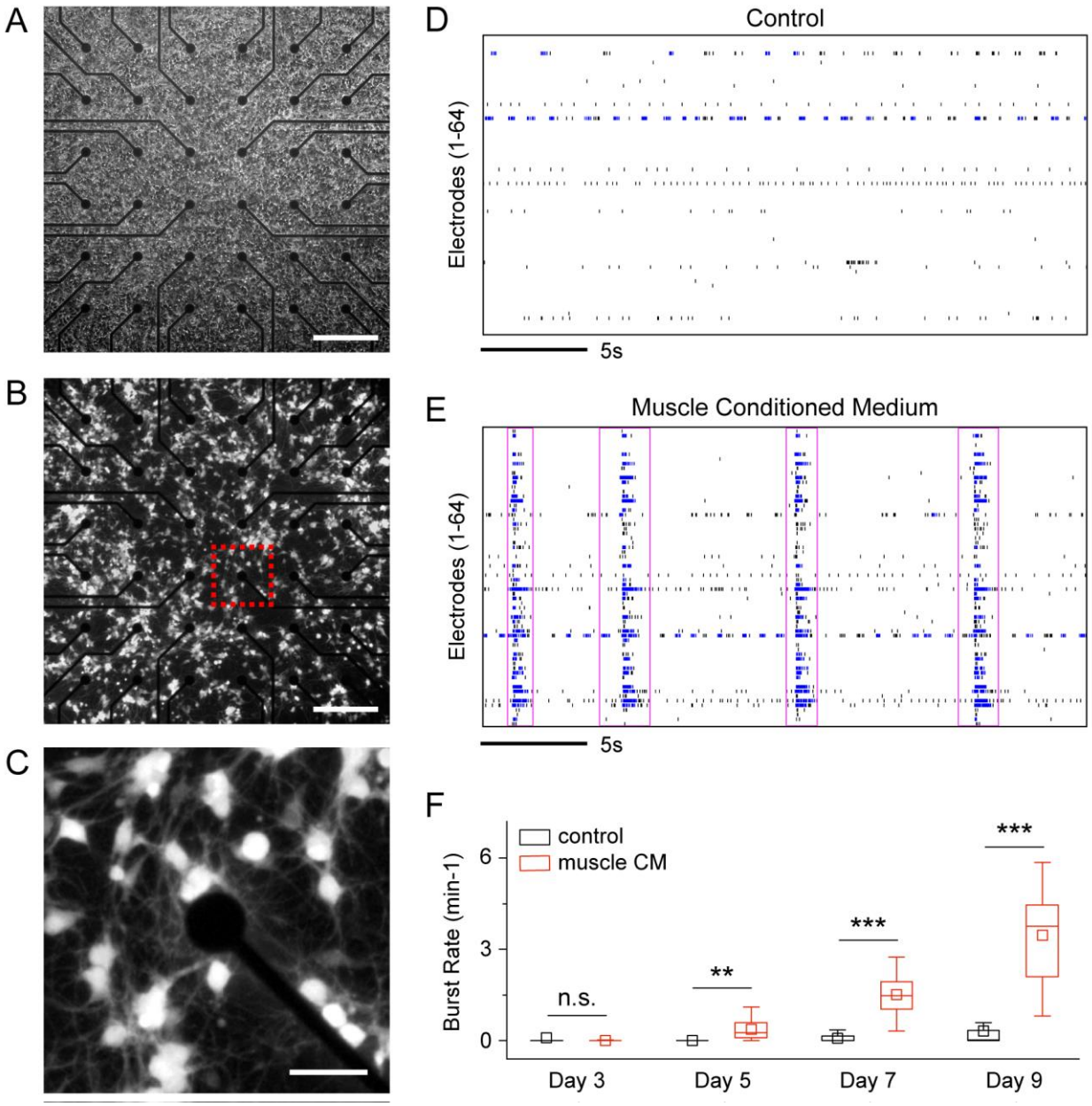

Figure 2.7: Muscle secreted factors delivered by CM facilitate spontaneous firing and network formation by neurons. (A) Phase contrast image of an MEA culture of cells obtained by dissociating neurospheres. Scale bar: 250 μm. (B) GFP image of the same culture, showing the Hb9-GFP^{+} MNs. Scale bar: 250 μm. (C) Zoomed-in view of the region outlined by dashed lines in B. Scale bar: 50 μm. (D-E) Raster plots of MEA recordings of representative samples from (D) control and (E) muscle CM groups at day 9. Black dashes represent individual spikes, blue dashes represent bursts, and pink boxes outline synchronous bursts. (F) Time evolution of burst rate of neurons in control and muscle CM groups. Box plots represent 25th, 50th, and 75th percentiles with whiskers representing 1.5x inter-quartile range, values are average burst rate per electrode over a 10-minute recording from the entire well, n=12 wells each for control and muscle CM at each day, **$p<0.005$ and ***$p<0.0005$ (Student's t-test).

2.5 Summary and conclusions

We have developed a relatively simple yet versatile 3D co-culture platform as a testbed for neuromuscular bioactuator development. Tissue-engineered skeletal muscle strips are anchored to compliant pillars which allow quantifying muscle contraction forces. These muscle strips are co-cultured in a compartmentalized setting with optogenetic mouse embryonic stem cell-derived neurospheres containing motor neurons. Motor neurons extend neurites preferentially toward the muscles, likely guided by muscle-secreted soluble factors, and form functional NMJs. Our methodology for the *in vitro* development of neuromuscular units on a compliant and 3D bioactuator platform will form the basis of the biohybrid swimmer design which will be presented in Chapter 3.

Using our platform in conjunction with MEA electrophysiology, we investigated the roles of activity-dependent and soluble factor-mediated reciprocal interactions in the co-development of muscle tissues and neural networks. Taken together, our results illustrate synergistic outcomes of neuron-muscle interactions during *in vitro* neuromuscular development (Fig. 2.8): Muscles secrete soluble factors which enhance spontaneous neural firing and the development of neural networks with synchronous bursting patterns. Neural firing in turn facilitates muscle contractility and the corresponding maturation of contractile apparatus. Our findings illustrate the potential value of identifying mechanisms for modulating these reciprocal interactions for the development of future neuromuscular bioactuators that can achieve predictable and tunable motor patterns.

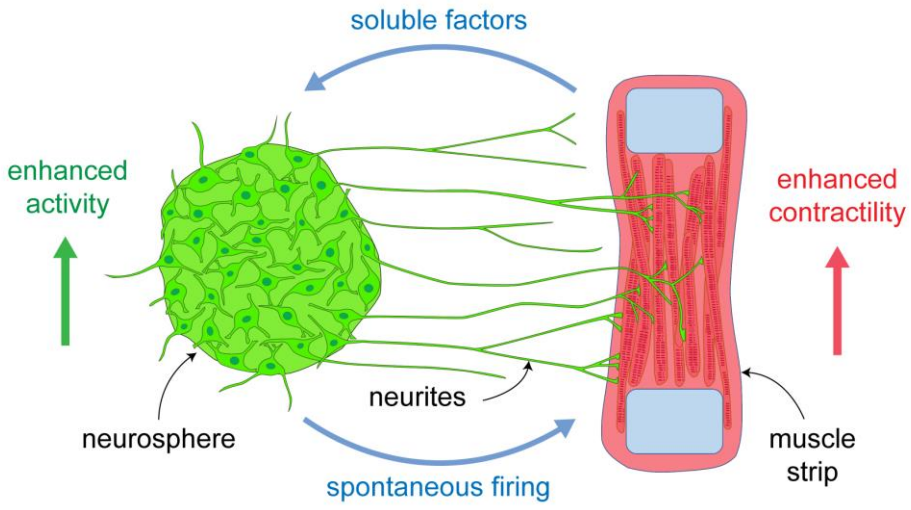

Figure 2.8: Conceptual illustration of the synergistic interactions between co-developing neural networks and muscle tissues, and the functional outcomes of these interactions.

2.6 Materials and methods

2.6.1 Cell culture

C2C12 skeletal myoblasts and NIH/3T3 fibroblasts (both from ATCC) were maintained below 70% confluency in muscle growth medium consisting of high-glucose Dulbecco's modified Eagle's medium (DMEM), supplemented with 10% v/v fetal bovine serum (FBS), and 2 mM L-Glutamine. To facilitate myotube formation by C2C12, they were cultured in muscle differentiation medium consisting of high-glucose DMEM, supplemented with 10% v/v horse serum, and 2 mM L-Glutamine (all reagents from Gibco). All C2C12 and NIH/3T3 cells were used at passage number 5. The optogenetic mouse ESC line $ChR2^{H134R}$-HBG3 Hb9-GFP [38], a generous gift from Prof. Roger Kamm's lab, Massachusetts Institute of Technology, MA, were maintained in undifferentiated state on a feeder layer of CF-1 mouse embryonic fibroblasts (Applied Stem Cell) in ESC growth medium consisting of EmbryoMAX DMEM (EMD Millipore), supplemented with 15% v/v ESC-qualified FBS (Gibco), 1X Nonessential Amino Acids (Gibco), 1X EmbryoMAX nucleosides (EMD Millipore), 2 mM L-Glutamine (Gibco), 0.1 mM β-mercaptoethanol (Gibco), and 10^3 units/ml leukemia inhibitory factor (EMD Millipore). Neurospheres with MNs were obtained by differentiating ESCs using an established protocol [63]. On day -6 (*i.e.*, 6 days before initiation of co-culture), ESCs were plated in a tissue culture dish in neural differentiation medium (NDM) consisting of Advanced DMEM/F-12 and Neurobasal medium mixed 1:1 by volume, supplemented with 10% v/v KnockOut serum replacement, 2 mM L-Glutamine, and 0.1 mM β-mercaptoethanol (all from Gibco). Cells were allowed to aggregate into embryoid bodies (EBs) in NDM for 2 days. On day -4, floating EBs were collected and plated in a new dish in NDM supplemented with 1 μM retinoic acid (RA) (Sigma Aldrich) and 1 μM sonic hedgehog agonist purmorphamine (PM) (EMD Millipore) to direct differentiation to MNs. Cells were allowed to differentiate for 3 days. On day -1, EBs were collected and re-plated in NDM supplemented with fresh 1 μM RA and 1 μM PM, as well as 10 ng/ml glial derived neurotrophic factor (GDNF) (Neuromics) and 10 ng/ml ciliary neurotrophic factor (CNTF) (Sigma Aldrich). On day 0, EBs (now neurospheres) were collected and seeded either into the PDMS platform for co-culture or dissociated and seeded onto MEAs for electrical recordings, in NDM supplemented with GDNF and CNTF at 10 ng/ml each.

2.6.2 PDMS platform fabrication

PDMS platforms were fabricated using microfabricated silicon molds and manual post-processing (Fig. 2.9). Silicon wafers were patterned by photolithography, etched using the Bosch process, and subsequently coated with polytetrafluoroethylene to facilitate removal of PDMS from the mold. PDMS (Sylgard 184) base and cross-linker were mixed at 10:1 ratio by weight, poured onto the silicon molds, and degassed using a vacuum desiccator. Samples were cured at 60°C for 12 hours and peeled off the silicon mold. To achieve the T-shape of the pillars, we attached caps onto the pillars, using a process adapted from previous studies [38], [40]. 200x150 µm pieces were cut from spin coated PDMS films of 30 µm nominal thickness using a razor blade mounted on an x-y-z stage. These caps were then manually glued onto the pillars using uncured PDMS.

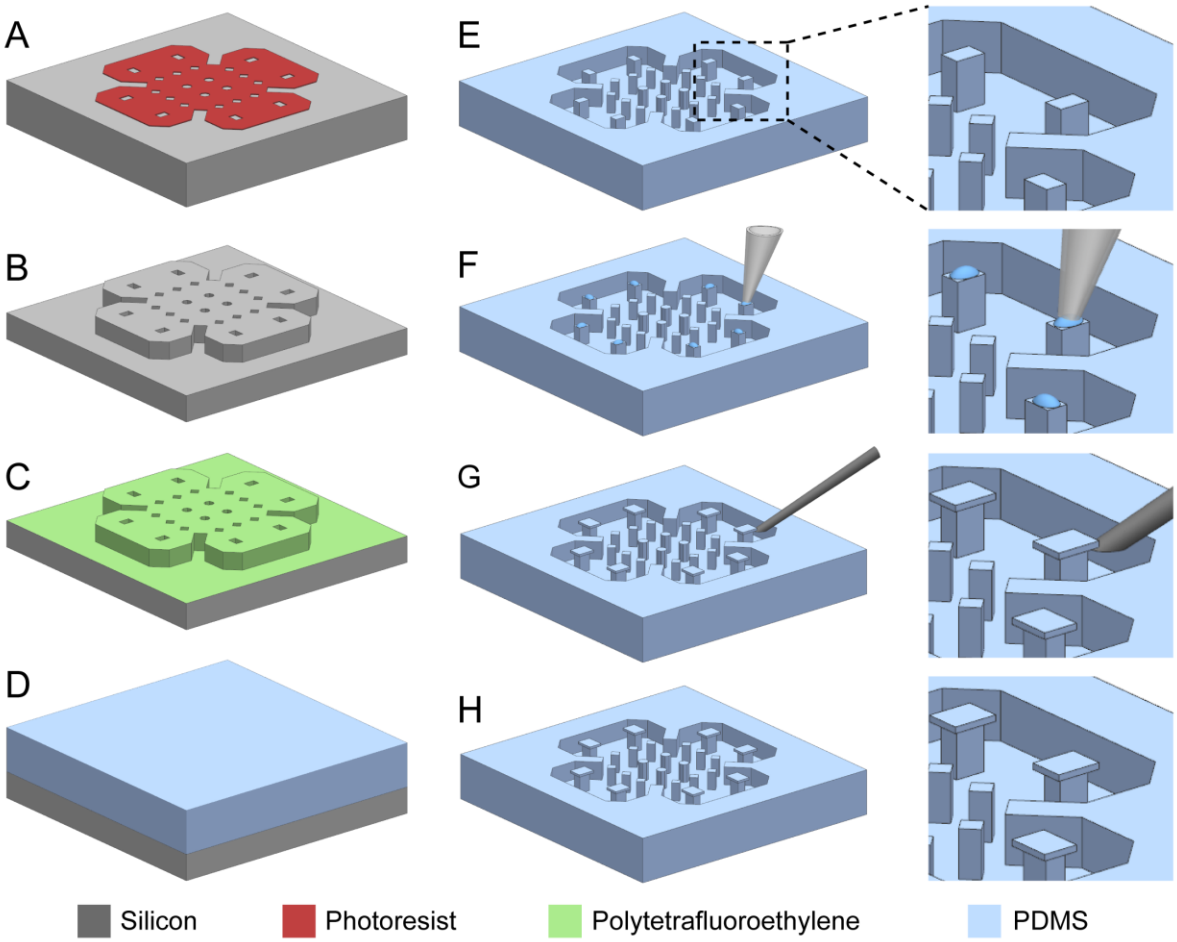

Figure 2.9: PDMS platform fabrication. Schematic of the microfabrication process flow illustrating (A) the photoresist pattern, (B) silicon etching, (C) polytetrafluoroethylene deposition, (D) PDMS casting, (E) cured and peeled PDMS structure, (F) application of uncured PDMS on top of the pillars and (G) placement of caps, and (H) the final platform.

2.6.3 Tissue seeding in PDMS platforms

Prior to tissue seeding, platforms were cleaned by first sonicating in ethanol for 20 minutes and then autoclaving at 121°C for 45 minutes while immersed in DI water. Platforms were then blow dried and sterilized by autoclaving at 121°C for another 45 minutes with 30 minutes drying time. For all tissue seeding procedures, ECM solution was prepared on ice by first neutralizing type I collagen from rat tail (Corning) with 1N sodium hydroxide, 10X phosphate buffered saline (PBS), and molecular biology grade water, and then mixing neutralized collagen thoroughly with growth factor reduced Matrigel (Corning). Collagen and Matrigel were used at final concentrations of 2 mg/ml each. To form muscle or fibroblast strips, C2C12 or NIH/3T3 were suspended in ECM solution at a density of $2.5x10^6$ cells/ml. Approximately 0.2 µl of cell-ECM mixture was pipetted into each target well and polymerized at room temperature for 30 minutes. Samples were then inundated in growth medium and incubated for 1 day while they compacted the ECM gel and formed a strip. After 1 day, culture medium was switched to muscle differentiation medium to facilitate myotube formation in muscle strips. Samples were kept in muscle differentiation medium for 6 days with daily medium replacements. To initiate neuron-muscle co-culture, medium was aspirated, the entire platform was filled with a fresh ECM solution, and a neurosphere with a diameter of 300-400 µm was selected and manually pipetted into the central well. ECM solution was then allowed to polymerize at room temperature for 30 minutes. Samples were incubated in NDM supplemented with GDNF and CNTF at 10 ng/ml each, with daily medium replacements until experiments were terminated.

2.6.4 Image acquisition and optical stimulation

All live imaging was performed on an Olympus IX81 inverted microscope (Olympus America) with a digital CMOS camera (Hamamatsu), mounted on a vibration isolation table. The microscope was equipped with an environmental chamber to maintain samples at 37ºC and 5% CO_2 during imaging. For muscle contraction assays, phase contrast images were taken at 100 frames per second using a 4X air objective to have the entire sample in the field of view. For optical stimulation, a GFP filter coupled to an X-Cite 120PC Q widefield fluorescent light source (Excelitas Technologies) was used to deliver blue light with 470 nm wavelength at 3.9 mW/mm^2 as measured by a power meter at the sample plane. Samples were stimulated with a 1-second-long bout of light by controlling the motorized shutter of the fluorescent light source.

2.6.5 Muscle strip force measurement

Pillar deflections caused by muscle contractions were measured from video recordings using the image analysis software Tracker (http://physlets.org/tracker). To compute contraction force, measured deflections were multiplied by pillar stiffness. Pillar stiffness was estimated using a finite element model of the PDMS pillar created in Comsol Multiphysics (Fig. 2.10A). The elastic modulus of PDMS was measured by nano-indentation as 1.72±0.14 MPa (mean ±SD, n=6). Pillar width, thickness, height, and cap height were measured by optical microscopy as 128.9±1.1 µm, 90.0±1.2 µm, 192.7±5.1 µm, and 26.6±2.1 µm, respectively (mean ±SD, n=30). A linear elastic constitutive model was used with 1.72 MPa elastic modulus and 0.5 Poisson's ratio. Side views of the muscle strips show that muscles wrap around the pillar caps (Fig. 2.10B). Thus, to approximate experimental loading conditions in the finite element model, force was applied to the pillar cap, and fixed boundary condition (zero displacement) was prescribed at the bottom surface of the pillar. Pillar geometry was meshed using tetrahedral elements (Fig. 2.10C). Forces with magnitudes ranging from 0 µN to 200 µN were applied and the resulting pillar deformation was monitored (Fig. 2.10D). Slope of the force-displacement curve (Fig. 2.10E), *i.e.*, pillar stiffness, was found to be 4.0 µN/µm.

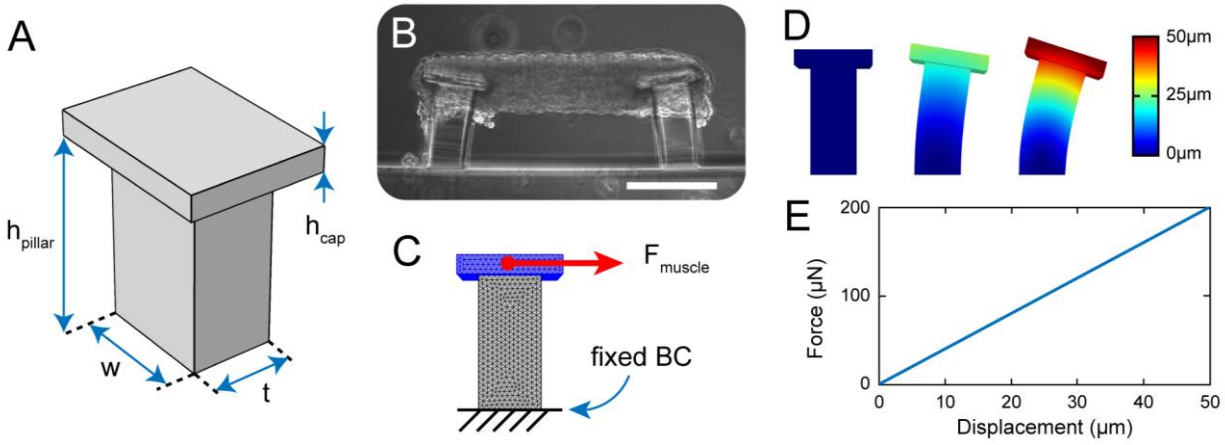

Figure 2.10: Pillar stiffness estimation. (A) Pillar structure created in FEM. (B) Phase contrast image of a representative muscle strip from the side view illustrating muscle strip attachment. Scale bar: 200µm. (C) Meshed pillar structure in FEM illustrating boundary and loading conditions. (D) Pillar deformation profiles upon application of (left) 0 µN, (middle) 100 µN, and (right) 200 µN force. Color bar shows displacement values. (D) Force-displacement curve obtained from FEM.

2.6.6 Immunofluorescence

To visualize muscle fibers and cross-striations, samples were fixed in 4% v/v paraformaldehyde in PBS for 4 hours at 4°C, permeabilized with 0.2% v/v Triton X-100 for 30 minutes at room temperature (RT), then incubated in blocking buffer consisting of 5% v/v goat serum, 1% w/v bovine serum albumin, and 0.05% v/v Tween-20 in PBS (all from Sigma Aldrich) for 2 hours at RT. Samples were then incubated overnight at 4°C in rabbit anti-α-actinin (1:250, Abcam) primary antibody diluted in blocking buffer, followed by 2 hours at RT in Alexa Fluor 488 goat-anti-rabbit IgG H&L (1:1000, Abcam) secondary antibody diluted in blocking buffer. Nuclei were stained with DAPI (5 µg/ml, Invitrogen) for 30 minutes at RT. To visualize neuromuscular units, AChRs were labeled with Alexa Fluor 647-conjugated α-bungarotoxin (2 µg/ml, Invitrogen) for 1 hour at 37°C, and samples were fixed, permeabilized, and blocked as before. Samples were then incubated overnight at 4°C in rabbit anti-β-tubulin III (1:1000, Synaptic Systems) primary antibody diluted in blocking buffer, followed by 2 hours at RT in Alexa Fluor 488 goat-anti-rabbit IgG H&L (1:1000, Abcam) secondary antibody diluted in blocking buffer. In all experiments, samples were rinsed 3x5 minutes with PBS between each incubation. Samples were embedded in ProLong Glass Antifade mountant (Invitrogen), covered with a glass coverslip, and allowed 24 hours at RT for the mountant to cure. Samples were then imaged on a Zeiss LSM 710 confocal microscope.

2.6.7 Conditioned medium

C2C12 were plated in tissue culture flasks, allowed to reach full confluency, and then cultured in muscle differentiation medium for 6 days with daily medium replacements. On day 6, muscle differentiation medium was aspirated, cells were rinsed 3 times with PBS, and incubated in 0.1 ml/cm^2 of Advanced DMEM/F-12 and Neurobasal medium mixed 1:1 by volume, supplemented with 2 mM L-Glutamine. After 24 hours, this basal CM was collected, filtered using syringe filters with 0.22 µm pore size, and neutralized to pH 7-7.4 using 1N sodium hydroxide. The full CM consists of basal CM, Advanced DMEM/F-12, and Neurobasal medium mixed 2:1:1 by volume, supplemented with 10% v/v KnockOut serum replacement, 2 mM L-Glutamine, 0.1 mM β-mercaptoethanol, and GDNF and CNTF at 10 ng/ml each. NDM with 10 ng/ml each of GDNF and CNTF was used as control.

2.6.8 MEA preparation, recording, and data analysis

12-well MEA plates (Axion BioSystems) contained 64 embedded 30 µm-diameter gold microelectrodes per well, spaced 200 µm apart. Plates were prepared for cell seeding according to manufacturer's protocol. Wells were coated with 0.1% polyethyleneimine for 1 hour at 37ºC then rinsed 3 times with PBS and allowed to air dry in a biosafety cabinet overnight. The following day, wells were coated with 20 µg/mL of laminin (Sigma Aldrich) for 2 hours at 37ºC before cell seeding. Neurospheres were dissociated in 0.05% w/v trypsin at 37ºC for ~5 minutes and passed through a 40 µm strainer to obtain a cell suspension. Dissociated cells were suspended in a 1:1 mixture of 20 µg/mL laminin and NDM supplemented with 10 ng/ml GDNF and 10 ng/ml CNTF, and seeded on MEA plates as a droplet centered over the electrode grid, at a density of 80,000 cells/well. Cells were incubated for 2 hours at 37ºC to allow for attachment, then inundated in NDM supplemented with 10 ng/ml GDNF and 10 ng/ml CNTF. Plates received medium changes every other day. Electrical activity on the MEAs was recorded using the Maestro system and AxIS software (both from Axion BioSystems), using the following settings: band-pass filter (Butterworth, 300-5000 Hz), spike detector (adaptive threshold crossing, 8xSD of RMS noise), burst detector (100 ms maximum inter-spike interval, 5 spikes minimum, 10 spikes minimum for network bursts, 10 s mean firing rate detection window). Recordings were performed daily for 15 minutes at 37°C. Raw files were processed offline, skipping the first 5 minutes of each recording as an acclimation period. Raster plots were generated using the Neural Metric tool (Axion BioSystems).

CHAPTER 3: BIOHYBRID SWIMMER ACTUATED BY NEUROMUSCULAR UNITS

This chapter is adapted from a previous publication[†].

3.1 Development of neuromuscular units on a free-standing scaffold

In the previous chapter, we have demonstrated the *in vitro* development of functional neuromuscular units formed by stem cell-derived motor neurons and tissue engineered muscles. Our results showed that this *in vitro* system successfully recapitulates the synergistic interactions between neurons and muscles that are predominant in the natural development of neuromuscular units *in vivo* [42]. In this chapter, we implement our methodology on a modified experimental platform to design and build a biohybrid swimmer at low Reynolds number actuated by on-board neuromuscular units.

The neuromuscular units established in the 3D co-culture platform of Chapter 2 were in the form of a free-standing tissue tethered to compliant pillars. However, the pillars were anchored at their base to a rigid substrate. To build a swimmer capable of untethered locomotion, it is necessary for the co-culture scaffold itself (*i.e.*, the body of the swimmer) to be free-standing. Thus, we begin this chapter by building a test platform to develop and characterize neuromuscular units on a free-standing scaffold. Fig. 3.1 illustrates our experimental procedure for forming functional neuromuscular units on a free-standing scaffold. More detailed descriptions and step-by-step illustrations of the procedures are presented in Section 3.6 Materials and methods.

The free-standing test scaffold consists of a structure with a hollow cavity to house a neurosphere and two compliant "legs" to anchor the muscle tissue. This scaffold is assembled with a spacer and two temporary tissue seeding molds which create a cavity around the legs to facilitate the seeding of the myoblast-ECM mixture (Fig. 3.1A). Once the myoblast-ECM mixture is compacted, the temporary seeding molds are removed, resulting in a muscle strip bridging the two compliant legs. We designed the shape of the legs to groove inwards at the free ends to trap the muscle strip at a prescribed location (Fig. 3.1B). Muscle cells are then allowed to differentiate for 6 days to form contractile myotubes within the muscle strips. In separate culture, neurospheres containing optically excitable motor neurons are obtained by directed differentiation of

[†] [43] O. Aydin *et al.*, "Neuromuscular actuation of biohybrid motile bots," *Proc. Natl. Acad. Sci.*, vol. 116, no. 40, pp. 19841–19847, 2019.

optogenetic mouse embryonic stem cells [38], [63] (Fig. 3.1C). To initiate co-culture, the scaffold, along with the muscle strip, are covered with fresh ECM and a neurosphere is seeded into the hollow cavity. The new ECM gel covering the scaffold and the tissues provides a continuous medium through which the neurons can extend neurites towards the muscle strip (Fig. 3.1D).

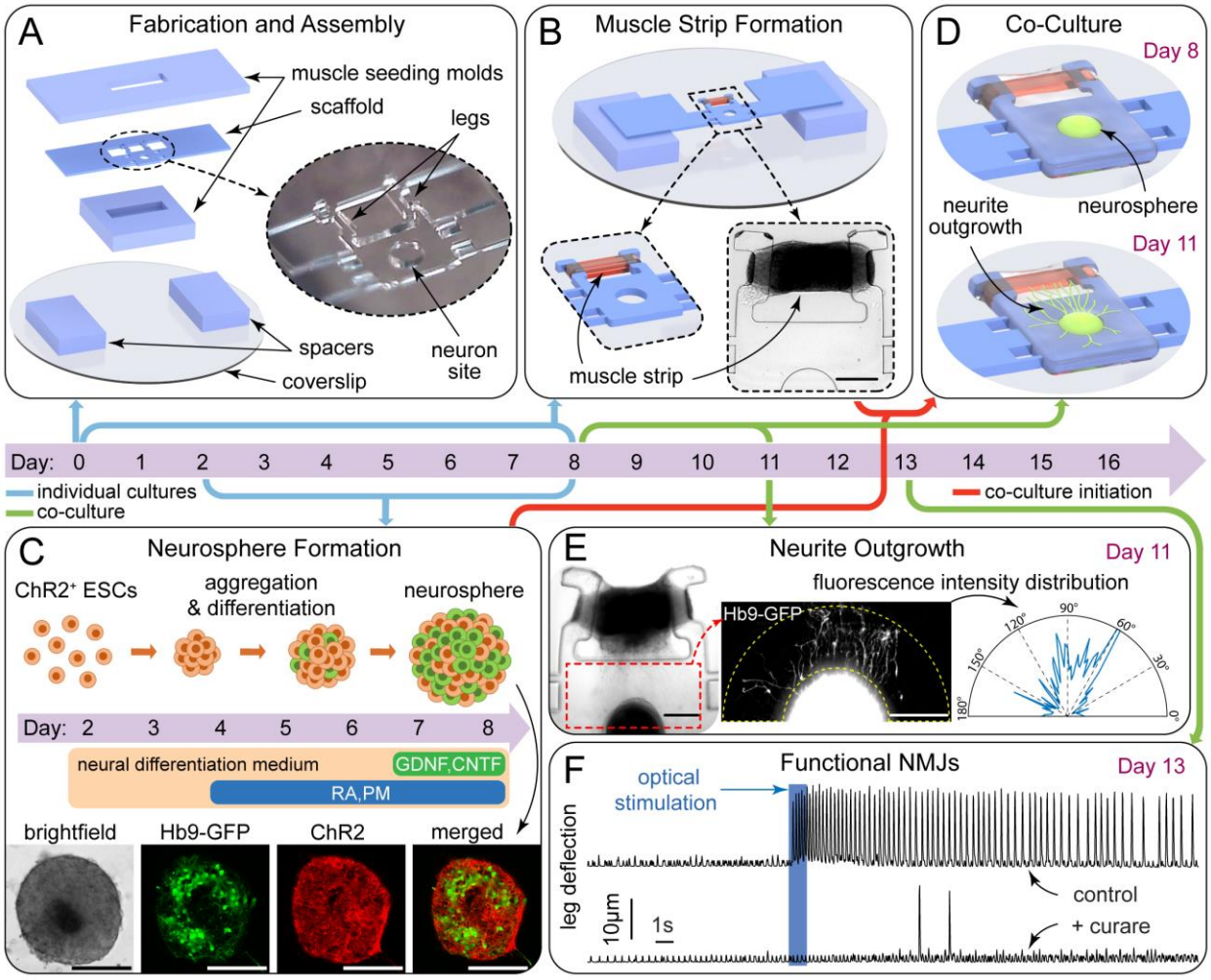

Figure 3.1: Timeline of neuromuscular bioactuator development on a free-standing and compliant scaffold. (A) Day 0: PDMS scaffold, spacers, and muscle seeding molds are assembled on a glass coverslip. (B) Muscle strip bridging the two legs is formed during the first 2 days in culture, then kept in muscle differentiation medium for the following 6 days. (C) Optogenetic mouse ESCs are differentiated in separate culture to obtain neurospheres, clusters of neural cells with photosensitive ChR2 ion channels and motor neurons expressing Hb9-GFP. (D) Day 8: Co-culture is initiated by embedding neurosphere and muscle in a continuous ECM gel. (E) Day 11: Neurite outgrowth pattern after 3 days in co-culture. Fluorescent intensity distribution around the neurosphere illustrates preferential neurite extension towards muscle strip. (F) Day 13 and onwards: Optical stimulation of neurons induces muscle contractions. Evoked contractions are not observed in the presence of 25 µM curare. All scale bars: 250 µm.

During the first 3 days of co-culture, we observe neurite outgrowth emanating from the neurosphere into the surrounding ECM. Neurite outgrowth was remarkably biased towards the muscle strip (Fig. 3.1E), most likely due to the action of muscle-secreted soluble factors [46], [47]. This preferential neurite outgrowth is in agreement with the results presented in Chapter 2 (see Section 2.3).

The motor neurons then innervate the muscle cells, forming NMJs. We characterized the functionality of the NMJs through a stimulation/inhibition assay. Under normal culture conditions, optical stimulation of motor neurons evoked periodic muscle contractions. This contraction pattern was absent when the NMJ inhibitor d-tubocurarine (curare) was applied. The occasional spontaneous twitches observed in the presence of curare suggest that its application did not hinder the contractility of the muscle cells, but that the NMJs were specifically targeted (Fig. 3.1D). Taken together, the ability to induce muscle contractions by optogenetic stimulation of motor neurons, and the absence of such evoked contractions under the application of curare, confirm the formation of functional neuromuscular units on our free-standing scaffold design.

3.2 Swimmer design

To demonstrate the application of our free-standing bioactuator (Fig. 3.1) to power a biohybrid machine, we developed a swimmer designed to operate at low Reynolds number. Low Reynolds number flows are the natural operating regime for swimmers of body sizes in the millimeter scale and below, swimming in water (or fluids with similar viscosity). Several mechanisms exist for achieving propulsion at low Reynolds number, one of which is to generate deformations of a slender and flexible filament (*i.e.*, a flagellum); a mechanism commonly used by biological swimmers including spermatozoa and many species of bacteria [64]–[66]. Flagellar propulsion has also been demonstrated in a biohybrid swimmer powered by cardiomyocytes [16].

To design our first swimmer prototype, we rely on insights and methods generated by previous studies. Here, we offer a qualitative physical description of the proposed design and its working mechanism, and proceed to build and test our prototype. A mathematical description of the problem and the process of formulating design strategies from first principles will be presented in Chapter 4, along with the appropriate tissue culture methods for experimental realization of the revised designs.

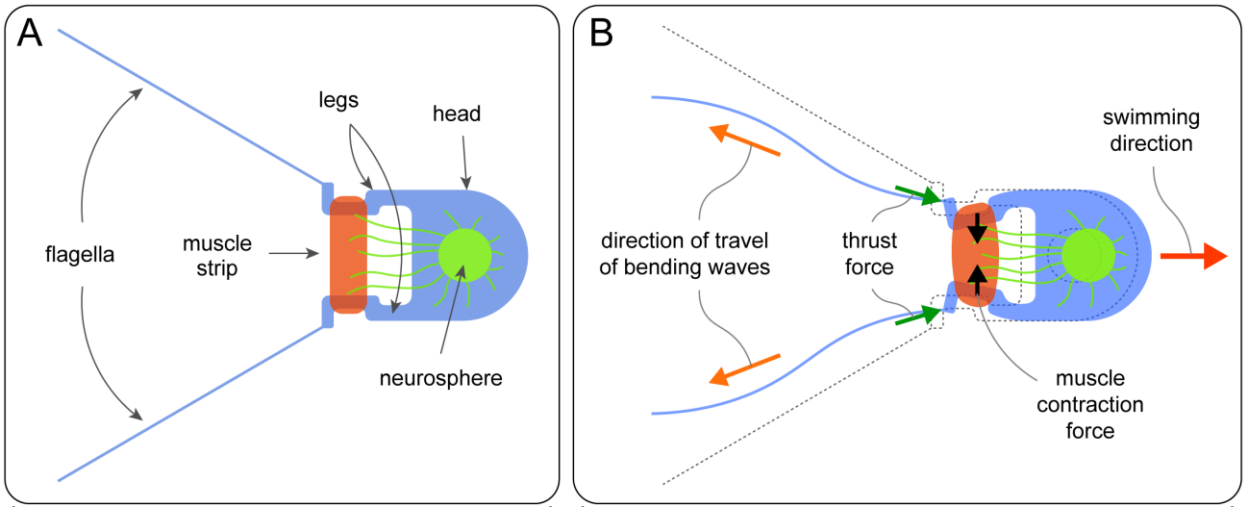

Figure 3.2: Flagellar swimmer prototype. (A) Schematic of the proposed design, illustrating two slender flagella attached to the scaffold legs. (B) Illustration of the proposed working mechanism. Dashed lines outline the undeformed configuration.

The proposed swimmer design and its working mechanism are illustrated in Fig. 3.2. The swimmer scaffold consists of the test platform of Fig. 3.1 with two modifications: The head is rounded to reduce drag, and two slender and flexible flagella (*i.e.*, "tails") are added to the tips of the legs (Fig. 3.2A). We chose to use two tails arranged symmetrically, since previous theoretical and computational models have suggested that an even number of tails arranged symmetrically leads to more efficient swimming; whereas an odd number of tails will result in lateral motions of the swimmer head, generating additional drag and impeding propulsion [43], [67].

When the muscle contracts and bends the legs, this leads to deflections at the base of the tails. The rest of the tail deforms passively as bending waves propagate along its length (Fig. 3.2B). Due to the anisotropy of viscous drag on slender filaments in low Reynolds number flow, these deformations generate thrust force along the longitudinal axes of the tails [68], and the flexibility of the tails ensure that these deformations are kinematically time-irreversible [69] (discussed in more detail in Chapter 4), thereby propelling the swimmer forward (Fig. 3.2B).

3.3 Untethered swimming powered by neuromuscular units

We proceeded to build and test our swimmer prototype. We fabricated the swimmer scaffold and established neuron-muscle co-culture using the methodology we had developed for the test platform of Fig. 3.1. Before releasing the swimmer, functionality of the neuromuscular units was assessed by optical stimulation, verifying the ability of muscle contractions to induce

deflection of the tails. We then released the swimmer (Fig. 3.3A) in a petri dish in co-culture medium and gently injected a mixture of Percoll and co-culture medium at the bottom of the dish. Percoll is a suspension of colloidal silica particles and has a density that is slightly higher than culture medium. Hence, the Percoll-medium mixture forms a layer of fluid at the bottom of the dish, generating buoyancy on the swimmer. Z-stack images confirmed that the swimmer is suspended to a height that is approximately 20 times the thickness of the swimmer scaffold, ensuring that no physical friction occurs between the swimmer and the substrate. Moreover, this clearance reduces potential hydrodynamic boundary effects [70]. Detailed descriptions of the fabrication and culture methods, including step-by step illustrations, and validation of the swimmer suspension by Percoll is presented in Section 3.6 Materials and methods.

After releasing the swimmer, we optically stimulated the motor neurons (1 Hz, 20% duty cycle) to evoke periodic muscle contractions, and the resulting deformations of the flagella propelled the swimmer forward (Fig. 3.3B). To quantify swimming velocity, we recorded videos of the swimmer and obtained its position in time by image processing. At rest (no muscle contractions) the swimmer drifted slowly (0.17 μm/s) due to the flow of culture medium caused by handling of the dish. Thus, for all subsequent analyses, the experimentally recorded position data were corrected for drift (see Section 3.6.6). Upon the onset of muscle contractions, the swimmer initially displayed a transient acceleration phase lasting approximately 1 second, followed by a steady-state phase with a constant time-averaged swimming velocity of 0.73 μm/s (Fig. 3.3C), corresponding to $Re = 2x10^{-3}$. Swimming speed was expected to be low for this initial prototype, given the targeted low Reynolds number regime, the relatively large body length (3.2 mm including head, legs, and tails), the viscous drag associated with the voluminous head, and sub-optimal actuation amplitudes. However, we note that despite being slow, the swimming velocity reported above is measured definitively, demonstrating actual untethered locomotion. Fluctuations in position recorded during the 5 second rest period had a root-mean-square amplitude of 0.45 μm whereas the distance traveled during steady-state swimming over 5 seconds is approximately 4.6 μm, an order of magnitude higher than the noise level.

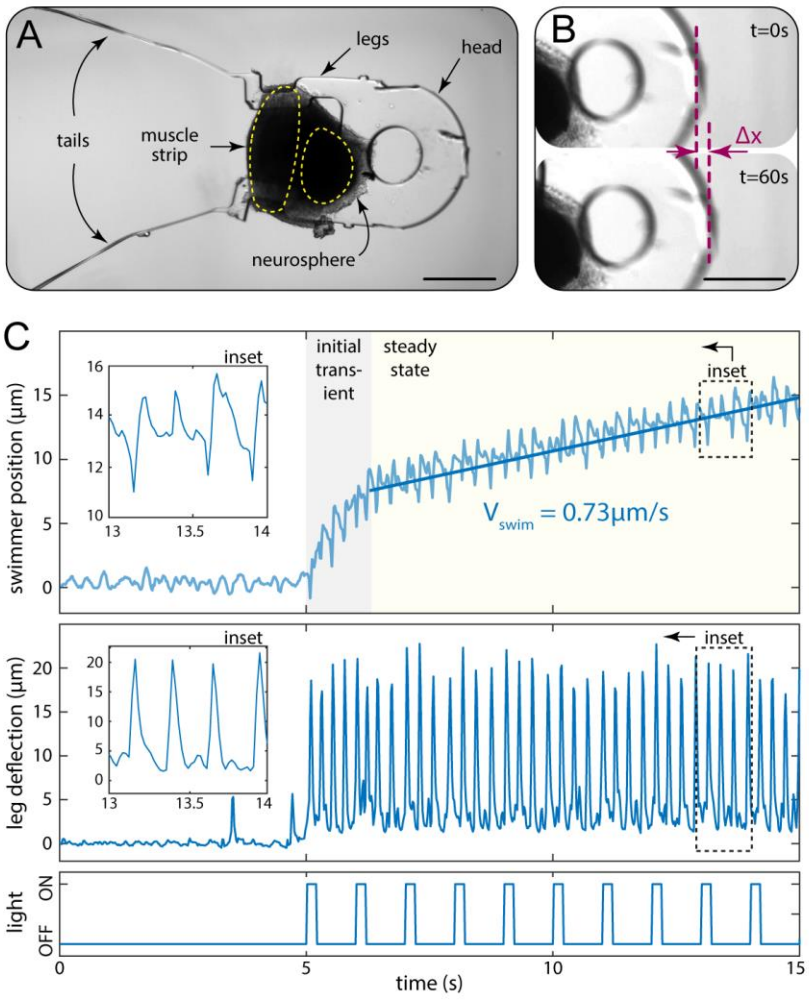

Figure 3.3: Untethered swimming driven by neuromuscular units. (A) Brightfield image of the swimmer after release from the anchors. The neurosphere is dislocated from its original seeding location due to tension generated between the muscle strip and the neurosphere. (B) Forward locomotion of the swimmer illustrated by the distance traveled in 60 seconds. (C) Experimental results showing: (top) swimmer position vs. time, (middle) leg deflection due to muscle contractions, (bottom) input optical signal. All scale bars: 500 μm.

3.4 Attenuation and recovery of bioactuator performance

The steady-state swimming shown in Fig. 3.3 was sustained for approximately 20 seconds, after which the magnitude and frequency of muscle contractions declined, and the swimmer decelerated, despite continuing optical stimulation of neurons (Fig. 3.4, left column). A possible reason for this attenuation of muscle activity is depletion of neurotransmitter vesicles at the NMJs. The pre-synaptic terminals of motor neurons host pools of neurotransmitter vesicles [71] which can be depleted due to repetitive stimulation [72]. Another possible reason is depletion of glucose or oxygen in the muscle cells. By allowing the system to rest, both resources can be replenished

since neurotransmitter vesicles can be recycled at the synapse [73] and nutrients in the surrounding medium can diffuse into the muscle tissue. Indeed, when we performed another recording after allowing the swimmer to rest for 1 minute, we observed that the initial acceleration and steady-state velocity were recovered (Fig. 3.4, middle column). This time, the steady-state velocity was sustained for approximately 8 seconds after which the swimmer decelerated again. In a third recording performed after an additional 10-minute break, swimming performance was sustained intermittently for approximately 30 seconds (Fig. 3.4, right column), similar to the first recording. The distance traveled during this third recording (~25 μm) was also comparable to that of the first swimming session. Taken together, these results show that the attenuation of muscle activity due to repetitive stimulation and the resulting decline in swimming performance is temporary and can be recovered by allowing the system to rest.

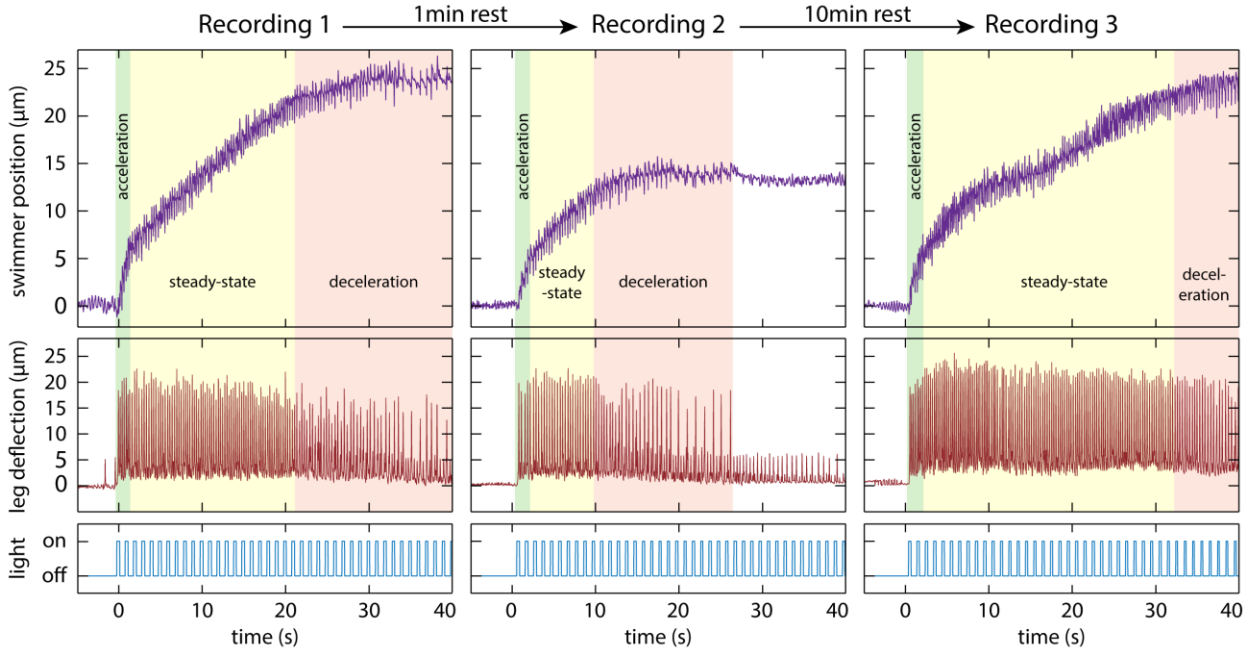

Figure 3.4: Attenuation and recovery of bioactuator output due to repetitive stimulation. Plots in the top, middle, and bottom rows illustrate the swimmer position vs. time, leg deflections due to muscle contractions, and optical stimulation regime, respectively. (Left column) Steady-state swimming is sustained for approximately 20 seconds, after which the muscle activity declines, and the swimmer decelerates. (Middle column) The next recording performed after allowing 1 minute rest shows that performance is recovered, but sustained for only about 8 seconds, followed by decline in actuator output and deceleration. (Right column) After allowing a longer 10 minutes rest period, steady-state swimming performance is recovered and sustained (albeit intermittently) for approximately 30 seconds before beginning to decelerate. In total, the swimmer travels a similar distance (25 μm) during the third recording as it did during the first.

3.5 Summary and conclusions

Neuronal actuation and control of muscle powered biohybrid machines is a currently emerging frontier in bioengineering. Since the nervous system interfaces with muscles through motor neurons, the first key milestone towards neuronal control is to establish biohybrid actuation with *in vitro* neuromuscular units. Here, we have developed an experimental platform where functional neuromuscular units are developed by co-culturing tissue engineered muscles with stem cell-derived motor neurons on a free-standing and compliant scaffold. Next, by modifying our initial test platform to include flagellar tails, we demonstrated an untethered biohybrid swimmer operating at low Reynolds number, driven by neuromuscular actuation.

We have characterized our neuromuscular bioactuator performance under continuous cyclic stimulation and showed that this leads to short term attenuation of bioactuator output, and performance is recovered when the system is allowed to rest. We postulated that this attenuation and recovery of bioactuator performance may be explained by the kinetics of neurotransmitter vesicle release or muscle metabolism. While our results so far are consistent with these potential explanations, further experiments are needed to provide more definitive evidence. Moreover, our results could also be explained by other mechanisms. One particularly intriguing hypothesis is that our *in vitro* neuromuscular units are undergoing short term habituation, a mechanism of implicit memory where the neural circuit learns to ignore a stimulus when it is applied repetitively [26]. This hypothesis will be discussed further in chapter 5.

3.6 Materials and methods

3.6.1 Cell culture

Neuron-muscle co-cultures on the free-standing bioactuator test platform and the swimmer scaffolds were established using C2C12 mouse skeletal myoblasts (ATCC) and the optogenetic mouse ESC line ChR2^{H134R}-HBG3 Hb9-GFP [38], a generous gift from Prof. Roger Kamm's lab, Massachusetts Institute of Technology, MA. Both cell types were cultured and differentiated using the same procedures and culture media formulations as described in Chapter 2, Section 2.6.1. Once established, the co-cultures were maintained co-culture medium consisting of Advanced DMEM/F-12 and Neurobasal medium mixed 1:1 by volume, supplemented with 10% v/v horse

serum (instead of KnockOut serum replacement which was used in the experiments in Chapter 2), 2 mM L-Glutamine, 0.1 mM β-mercaptoethanol (all from Gibco), 10 ng/ml GDNF (Neuromics), and 10 ng/ml CNTF (Sigma Aldrich).

3.6.2 Fabrication and assembly of PDMS scaffolds

PDMS structures were cast from microfabricated silicon molds. Silicon wafers were patterned by photolithography, etched using the Bosch process, and coated with polytetrafluoroethylene to facilitate removal of PDMS from the mold. Wafers were etched to a nominal depth of 100 µm for the co-culture test platforms and swimmer scaffolds, and to 300 µm for the spacers and muscle seeding molds. PDMS (Sylgard 184) base and cross-linker were mixed at 10:1 ratio by weight, pipetted into the molds, and allowed to spread. Trenches for slender features such as the legs and tails were filled by capillary mircomolding [74]. Samples were cured at 60°C for 12 hours and peeled off the silicon mold. The parts were then assembled on top of a glass coverslip with the co-culture scaffold placed on the spacers and sandwiched between the two muscle seeding molds (Fig. 3.5A-B). Scaffold assemblies were sterilized by autoclaving at 121°C for 45 minutes with 30 minutes drying time.

3.6.3 Tissue seeding on test platform

For all tissue seeding procedures, ECM solution was prepared on ice by first neutralizing type I collagen (Corning) with 1N sodium hydroxide, then mixing neutralized collagen thoroughly with Matrigel (Corning). Collagen and Matrigel were used at final concentrations of 2 mg/ml each. Fig. 3.5 shows a step-by-step illustration of the tissue seeding procedure on the free-standing bioactuator test platform. To form muscle strips, C2C12 myoblasts were suspended in ECM solution at a density of 2.5×10^6 cells/ml. Cell-ECM mixture was pipetted into the cavity formed around the legs by the muscle seeding molds (Fig. 3.5C), and allowed to gel at room temperature for 30 minutes. Samples were then inundated in muscle growth medium and incubated for 2 days. At day 2, the muscle seeding molds were removed, parts of the scaffold were cut out to allow free deflection of the legs (Fig. 3.5D-F), and culture medium was switched to muscle differentiation medium. Samples were kept in muscle differentiation medium for 6 days with daily medium replacements. To seed the neurosphere, culture medium was aspirated, fresh ECM solution was pipetted onto the scaffold, then a neurosphere with approximately 400 µm diameter was selected

and seeded into the hollow cavity on the scaffold (Fig. 3.5G). ECM solution was then allowed to gel at room temperature for 30 minutes (Fig. 3.5H) after which the samples were inundated in co-culture medium. Co-culture medium was replaced daily until experiments were terminated. The fresh ECM gel covering the scaffold and the tissues provides a continuous medium through which the neurons within the neurosphere can extend neurites towards the muscle strip (Fig. 3.5I).

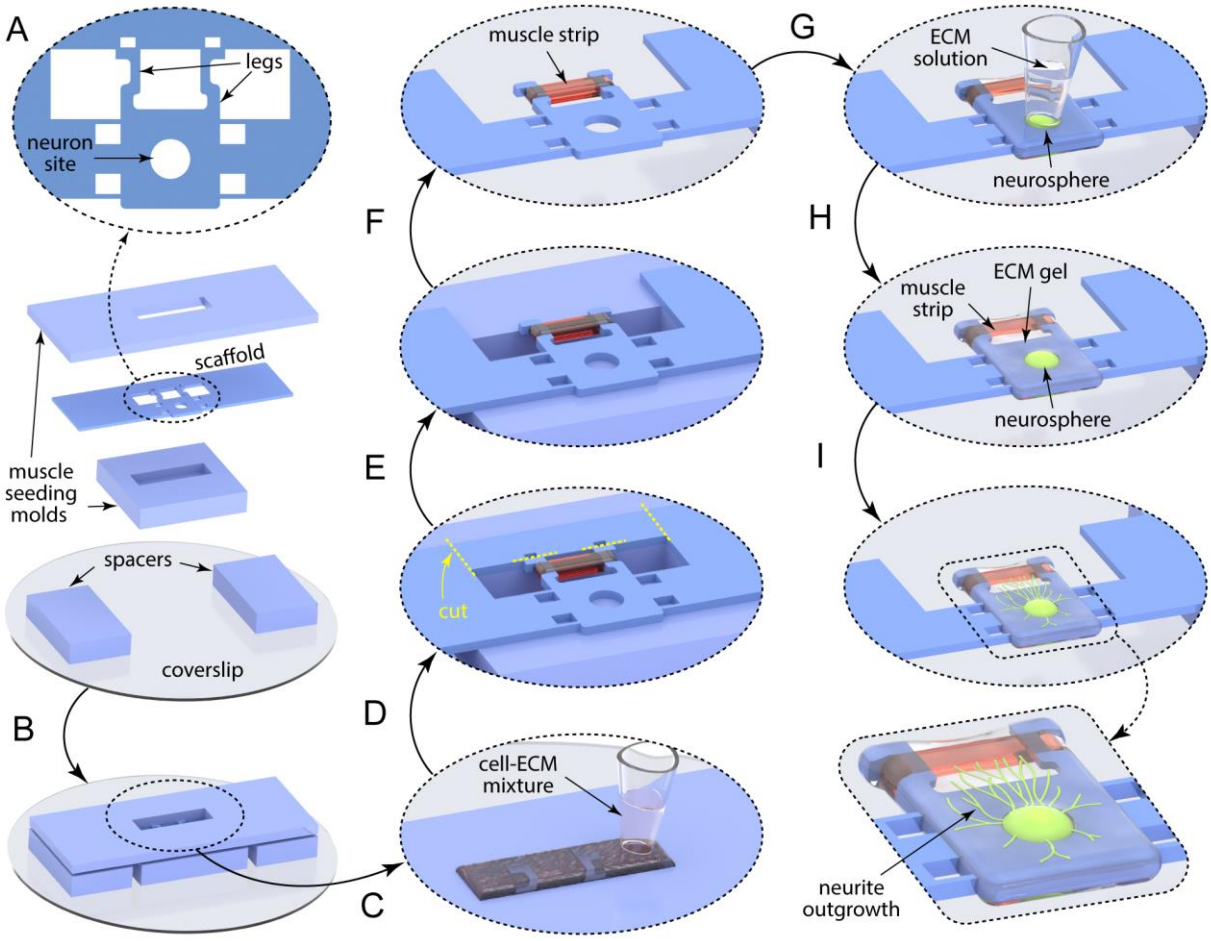

Figure 3.5: Schematic of neuron-muscle co-culture formation on free-standing scaffold. (A) The PDMS scaffold, muscle seeding molds, and spacers are fabricated and (B) assembled on a glass coverslip. (C) Myoblast-ECM mixture is seeded into the cavity formed by muscle seeding molds. (D) Top seeding mold is removed after gel compaction and (E) parts of the scaffold are removed by cutting along the dashed lines to allow free leg deflection. (F) Bottom seeding mold is removed. (G) The muscle strip and the scaffold are covered with liquid ECM, then a neurosphere is selected and seeded into the hollow cavity. (H) Upon gelation of ECM, we obtain co-culture on the free-standing scaffold where muscle strip and neurosphere are embedded in a continuous ECM gel which allows (I) neurite outgrowth from the neurosphere.

3.6.4 Swimmer fabrication, tissue seeding, and release

The swimmer scaffold design includes several modifications of the test platform, and the tissue seeding procedure was adjusted accordingly (Fig. 3.6). The head and legs of the swimmer have the same geometry as the test scaffold except for the swimmer head being rounded to reduce drag. Slender tails emanate from each leg and are attached at the ends to the scaffold via compliant springs (Fig. 3.6A). Neuron-muscle co-culture was developed on the swimmer scaffold following a similar procedure as for the test platform (Fig. 3.6B-F). To achieve untethered locomotion, the swimmer was released by cutting around the head and at the ends of the tails (Fig. 3.6F-G).

Once released, the swimmer was immersed in 10 ml co-culture medium in a 100 mm-diameter tissue culture dish. Then, 10 ml of a 1:1 mixture (by volume) of Percoll (Sigma Aldrich) and co-culture medium was carefully injected at the bottom of the dish to suspend the swimmer in fluid (Fig. 3.6G-H). To confirm that the swimmer is suspended to a sufficient height to prevent friction, we took z-stack images and measured the distance between the swimmer and the bottom of the dish. The bottom of the dish was scored manually using a glass pipette tip to identify when the bottom surface comes into focus. Z-stacks were taken at 10 μm intervals starting from below the dish up to a focal plane above the swimmer. Before adding Percoll-medium mixture, the swimmer was at a height of approximately 250 μm, comparable to the thickness of the swimmer scaffold (100 μm). After adding 10 ml Percoll-medium mixture, we allowed 30 minutes for the flow perturbations to diminish and then took z-stacks every 15 minutes for 6 hours. During this time, the swimmer remained suspended at a height of approximately 2 mm which is 20 times the thickness of the swimmer (Fig. 3.6I).

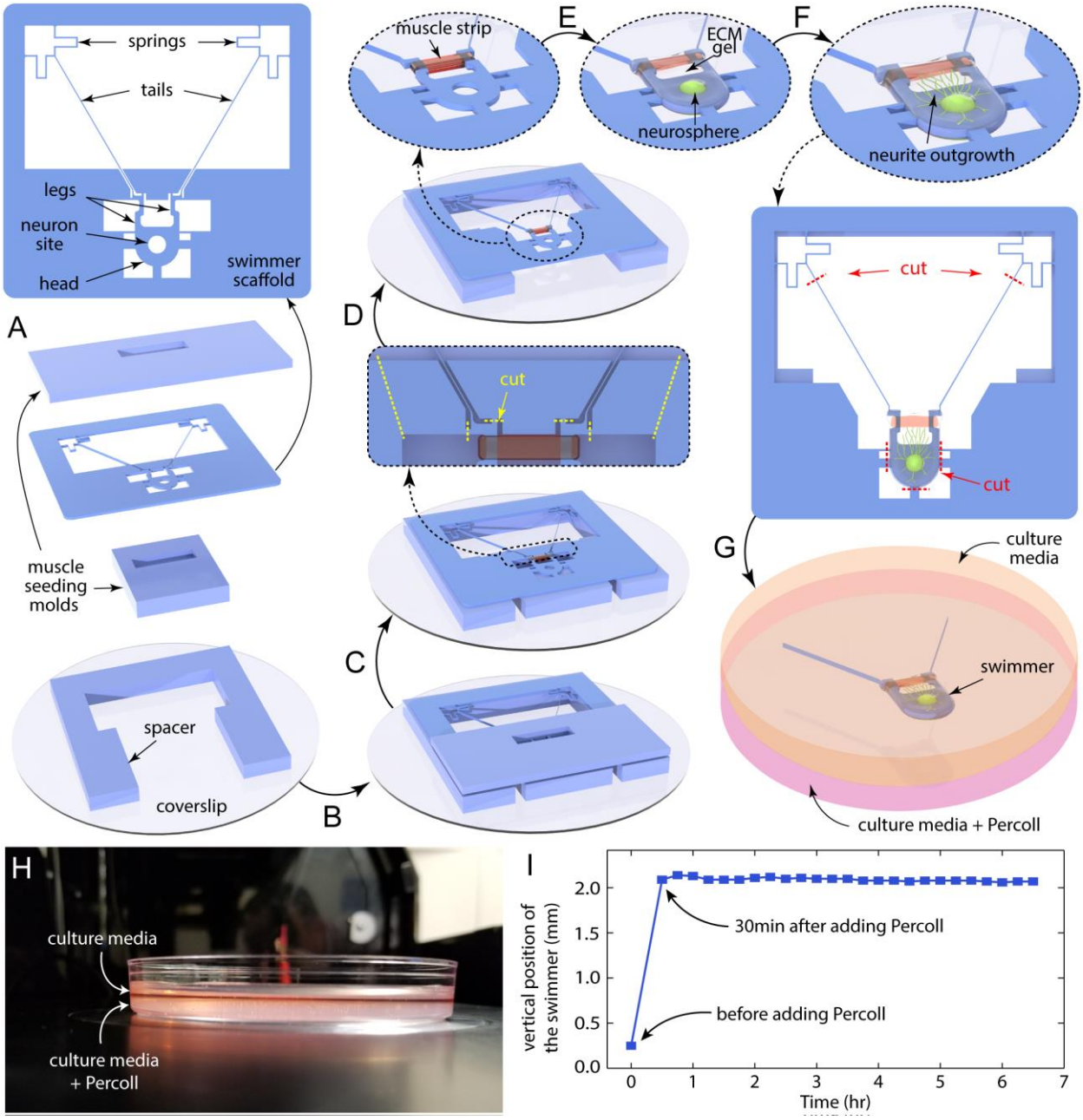

Figure 3.6: Schematic of modified procedure for neuron-muscle co-culture formation on the swimmer scaffold. (A) The swimmer scaffold, muscle seeding molds, and the spacer are fabricated and (B) assembled on a glass coverslip. (C) A muscle strip is formed, and the top seeding mold is removed. (D) Parts of the scaffold are removed by cutting along the dashed lines to allow free deflection of the legs, and the bottom seeding mold is removed. (E) A neurosphere is seeded in the hollow cavity on the head and the tissues are embedded in ECM gel to allow (F) neurite outgrowth towards the muscle strip. (G) The swimmer is released by cutting along the dashed lines and suspended in a dish between a layer of co-culture medium and medium-Percoll mixture. (H) Side view of the dish in which the swimmer is suspended between the two layers of fluid. (I) Measurements of the vertical distance between the swimmer and the bottom surface of the dish. The first data point corresponds to the distance measured before adding Percoll-media mixture.

3.6.5 Image acquisition, processing, and optical stimulation

All imaging was performed on an Olympus IX81 inverted microscope (Olympus America) with a digital CMOS camera (Hamamatsu), mounted on a vibration isolation table. The microscope was equipped with an environmental chamber to maintain samples at 37°C and 5% CO_2 during imaging. To visualize motor neurons, fluorescent images of Hb9-GFP$^+$ MNs were taken using a GFP filter coupled to an X-Cite 120PC Q widefield fluorescent light source (Excelitas Technologies). To record muscle contractions and swimming, brightfield images were taken at 100 frames per second using a 4X air objective. Leg deflections and the swimmer's position during swimming were measured from video recordings using the image processing software Tracker (http://physlets.org/tracker). Optical stimulation was performed using the fluorescent light source and GFP filter, delivering blue light at 470 nm wavelength with 3.9 mW/mm^2 intensity as measured by a power meter at the sample plane. Samples were stimulated with 200 ms or 1000 ms exposure by controlling the shutter of the fluorescent light source.

3.6.6 Correction of swimmer position for drift

While the swimmer is kept free-floating in a dish, it drifts relatively slowly due to fluid flow caused by manual handling of the petri dish. We account for this drift by correcting the position data that is obtained from videos. We recorded videos of the swimmer continuously during the rest phase and the swimming phase. Given that the diameter of the dish (100 mm) is much larger than the body size of the swimmer (~1 mm), we assume that the swimmer experiences a uniform and constant drift flow. Thus, the scalar components of drift velocity $u_{x,drift}$ and $u_{y,drift}$ were computed from linear fits to the corresponding position component-time data during the 10 second drift period before initiation of active swimming. The components of position data during swimming were then corrected as $x_{corr} = x - u_{x,drift}(t - t_{start})$ and $y_{corr} = y - u_{y,drift}(t - t_{start})$ where x and y are the original data, x_{corr} and y_{corr} are the corrected positions, and t_{start} is the time of initiation of active swimming. The net swimmer position is computed as $r_{corr} = \sqrt{x_{corr}^2 + y_{corr}^2}$ and swimming velocity is computed from the linear fit to the position-time data during the steady-state swimming phase.

CHAPTER 4: DESIGN STRATEGIES FOR IMPROVING SWIMMING PERFORMANCE

4.1 Mechanism of flagellar propulsion at low Reynolds number

A major drawback of our initial neuromuscular swimmer prototype is its relatively low swimming speed (0.02% of body length per second). The aim of this chapter is to derive and evaluate design strategies to significantly improve swimming performance. We begin this chapter with a physical description of the mechanism of flagellar propulsion at low Reynolds number.

In our swimmer design, thrust is provided by the flagellar tails which are actuated at their base by the motions generated by muscle contractions. These motions can be decomposed into translation and rotation with amplitudes $\delta(t)$ and $\theta(t)$, respectively (Fig. 4.1A-B). For a flexible tail, these displacements and rotations at the base of the tail lead to bending waves propagating along its length [75]–[78]. When a slender and flexible filament is actuated in this manner in a viscous fluid, it can generate thrust *locally* along the longitudinal direction (with respect to the undeformed configuration) due to the drag anisotropy on slender bodies at low Reynolds number [68], [75]. The viscous drag force acting on a body in low Reynolds number flow is generally expressed as a product of the drag coefficient and the velocity. For slender filaments (*i.e.*, cross-sectional dimensions $\ll$ length), the drag coefficients perpendicular and parallel to the filament, $\zeta_\perp$, and $\zeta_\parallel$, respectively, are given by slender body theory [79] as:

$$\zeta_\perp \cong \frac{4\pi\mu}{\ln(L/r)} \tag{4.1a}$$

$$\zeta_\parallel \cong \frac{2\pi\mu}{\ln(L/r)} \tag{4.1b}$$

where μ, L, and r are the fluid viscosity, filament length, and filament radius, respectively. As equation 4.1 shows, slender body theory predicts $\zeta_\perp \cong 2\zeta_\parallel$. Consequently, when a bending wave propagates along the length of the tail, an infinitesimal segment of the tail that is moving vertically while it is oriented at an angle to the horizontal axis (see Fig. 4.1C), will experience a drag force which has a component along the horizontal direction (longitudinal direction of the undeformed tail). This component of drag is the local thrust force (f_p in Fig. 4.1C).

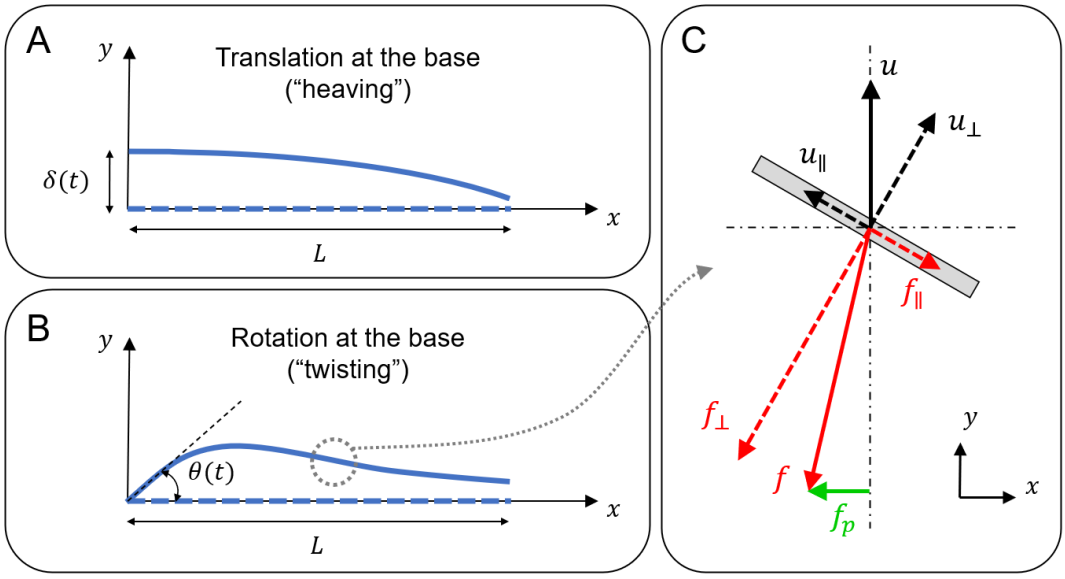

Figure 4.1: Thrust force is generated locally due to drag anisotropy as bending waves propagate along the tail length. (A-B) Depictions of the two modes of actuating the tails by (A) translating and (B) rotating at the base. Dashed line represents the undeformed configuration of the tail and solid line represents the deformed configuration. (C) Schematic showing the local velocity and force components on an infinitesimal segment of the tail.

Generating local thrust forces, however, does not guarantee swimming. An important and well-known property of low Reynolds number flows is kinematic reversibility, a symmetry property which arises from the linearity and time independence of the Stokes equations [68]: When the motion (*i.e.*, the velocity and rotation rate) of a body in low Reynolds number flow is reversed, the entire flow velocity and pressure fields, and the corresponding hydrodynamic forces and torques acting on the body, are also reversed instantaneously. This symmetry property has a key consequence for swimming at low Reynolds number, commonly known as the Scallop Theorem: For a swimmer that is generating cyclic body deformations, to produce net thrust averaged over the cycle, the sequence of shapes that the swimmer's body goes through must be *time-irreversible* [69]. Consider the schematic in Fig. 4.1C which shows the velocity of a segment of the tail, and the corresponding local drag force acting on it, as the tail is moving "forward". If this segment of the tail goes through the same geometric configuration when the tail moves "backward" to complete the cycle, then the velocity and force vectors will be reversed. The corresponding local thrust force will be equal and opposite to the one that was generated during the forward stroke, thereby cancelling it out. If this holds for all segments of the tail over the entire cycle, then no net thrust will be generated and the swimmer will oscillate in place.

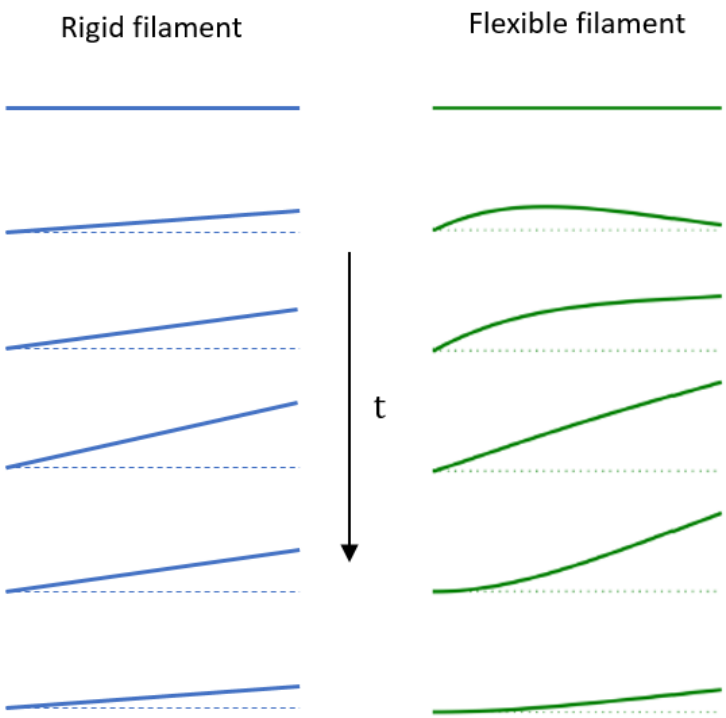

Figure 4.2: Comparison of deformation sequences of rigid and flexible filaments in viscous fluid that are actuated by rotating at the base.

One of the ways to break the time symmetry is to use a flexible tail [69]. This is illustrated qualitatively in Fig. 4.2 by comparing the deformations of rigid and flexible filaments over one cycle as they move in a viscous fluid, actuated by rotating at their base. The sequence of shapes that the rigid filament goes through is the same when viewed backward in time (*i.e.*, time-reversible), whereas the flexible filament goes through time-irreversible deformation. We will show in Section 4.3 below that optimum flexibility is achieved when the transverse drag force and the elastic restoring force are comparable in magnitude.

4.2 Elasto-hydrodynamic model

To guide our investigation of potential design strategies to improve swimming performance, we first develop a mathematical model of the elasto-hydrodynamics of the swimmer to predict the swimming speeds of candidate designs.

As the bending waves propagate along the filament, each infinitesimal segment of the filament moving in the transverse direction with a local velocity of $\partial y/\partial t$, experiences a viscous drag force that resists its motion, given by,

$$F_D = \zeta_\perp \frac{\partial y}{\partial t} \tag{4.2}$$

where $\zeta_\perp$ is the transverse viscous drag coefficient (given by equation 4.1a). Additionally, each segment experiences an elastic restoring force (or "bending force"), given by,

$$F_E = -EI \frac{\partial^4 y}{\partial x^4} \tag{4.3}$$

where E and I are the elastic modulus and moment of inertia of the filament, respectively. Balancing these forces yields the governing equation for the elasto-hydrodynamics of the filament:

$$-EI \frac{\partial^4 y}{\partial x^4} + \zeta_\perp \frac{\partial y}{\partial t} = 0 \tag{4.4}$$

We obtain the deformation pattern of the filament, $y(x, t)$ by numerically solving equation 4.4 in MATLAB using the finite difference method, with the following boundary conditions: Base of the filament is actuated with,

$$y(0, t) = \delta(t) \tag{4.5a}$$

$$\frac{\partial y}{\partial x}(0, t) = \tan\left(\theta(t)\right) \tag{4.5b}$$

and the end of the filament is free, therefore experiencing zero force and moment:

$$\frac{\partial^2 y}{\partial x^2}(L, t) = 0 \tag{4.5c}$$

$$\frac{\partial^3 y}{\partial x^3}(L, t) = 0 \tag{4.5d}$$

Once $y(x,t)$ is computed, the total thrust force generated by the entire filament at a given time can be found by,

$$F_P(t) = \int_0^L (\zeta_\perp - \zeta_\parallel) \frac{\partial y}{\partial x} \frac{\partial y}{\partial t} dx \tag{4.6}$$

During swimming, this total thrust force is resisted by viscous drag. The drag force on the tail is primarily along the longitudinal direction since the tails are oriented mostly parallel to the direction of swimming:

$$F_{D,tail}(t) \cong \zeta_\parallel \, L \, u(t) \tag{4.7}$$

where $u(t)$ is the swimming velocity. Estimating the drag force acting on the rest of the swimmer's body is slightly more challenging since the assembly of the head, legs, and tissues has an irregular shape. Here, we approximate this shape as a sphere, and use Stokes' Law:

$$F_{D,body}(t) \approx 6\pi\mu \, R_{body} \, u(t) \tag{4.8}$$

where R_{body} is the equivalent radius of the swimmer body. Although Stokes' Law is strictly valid for a sphere, drag on non-spherical objects in low Reynolds number flow can be accurately modeled by the same expression multiplied by a scalar correction factor, often determined empirically [80]. This is mathematically equivalent to tuning the value of R_{body}. In a previously published study, the performance of our swimmer prototype of Chapter 3 was accurately simulated by a computational model that used this approximation and estimated R_{body} based on the length, width, and height of the swimmer body [43].

For a two-tailed swimmer design, force balance requires:

$$2F_P = 2F_{D,tail} + F_{D,body} \tag{4.9}$$

Substituting the expressions in equations 4.6, 4.7, and 4.8, and solving for velocity, we obtain:

$$u(t) \cong \frac{2\int_0^L (\zeta_\perp - \zeta_\parallel)\frac{\partial y}{\partial x}\frac{\partial y}{\partial t}\,dx}{2\zeta_\parallel L + 6\pi\mu\, R_{body}} \tag{4.10}$$

4.3 Physical insights: nondimensionalization and the Sperm number

This elasto-hydrodynamic model offers a means to predict swimming speed. To investigate possible design strategies, we first examine the mathematical model further, to gain physical insight. We can nondimensionalize equation 4.4 using $\tilde{x} = x/L$, $\tilde{y} = y/L$, and $\tilde{t} = \omega t$ where ω is the actuation frequency:

$$\frac{\partial^4 \tilde{y}}{\partial \tilde{x}^4} = -Sp^4 \frac{\partial \tilde{y}}{\partial \tilde{t}} \tag{4.11}$$

The nondimensional quantity Sp, is the Sperm number, given by,

$$Sp = L/\left(\frac{EI}{\zeta_\perp \omega}\right)^{-1/4} \tag{4.12}$$

The Sperm number characterizes the elasto-hydrodynamic behavior of the filament for any given actuation mode and amplitude. One of the physical interpretations of the Sperm number is that it is the ratio of the viscous drag force ($\sim \zeta_\perp \omega L$ per unit length) to the elastic restoring force ($\sim EI/L^3$ per unit length). In the limit $Sp \ll 1$, elastic restoring force dominates, and the filament moves as a rigid rod (see Fig. 4.2). In this case, the net time-averaged thrust generated by the filament is zero due to the Scallop Theorem. A corollary of this analysis is that the flexible tails in our swimmer design are the only components that generate net thrust. The head and leg structures are at least three orders of magnitude more rigid and therefore operate in the $Sp \ll 1$ regime, generating no net thrust. In the $Sp \gg 1$ limit, the filament is too flexible and viscous drag forces dominate. The bending waves that travel along the length of the filament are dampened rapidly, and most of the length of the filament stays stationary, not contributing to thrust and producing additional drag.

The elasto-hydrodynamic theory therefore predicts that maximum swimming speed (for a given actuation mode and amplitude) will be achieved for an intermediate value of the Sperm number [67], [78], [81]–[83]. In other words, the tail with optimum flexibility is the one where the magnitudes of the elastic restoring forces and viscous drag forces are comparable, as mentioned in Section 4.1 above. Indeed, experimental results [84], [85], including that of our previously published study on the swimmer prototype of Chapter 3 [43], have confirmed the prediction that optimum swimming performance is achieved for an intermediate value of Sp. In our experiments, we varied the Sperm number by cutting the swimmer's tails to different lengths and measuring the steady-state swimming speed. A computational model (see Ref. [43]) was used to simulate the swimmer prototype and calculate swimming speed for different values of Sp. Fig. 4.3 shows a comparison of these results with the solution of the elasto-hydrodynamic model of this chapter. Both models and the experimental results illustrate a similar characteristic trend: As $Sp \to 0$, no net thrust is generated, due to the Scallop theorem, and swimming speed approaches 0. Maximum swimming speed is achieved for $Sp \cong 2$. For higher values of Sp, swimming speed drops since viscous drag begins to dominate and bending waves do not propagate effectively along the tail.

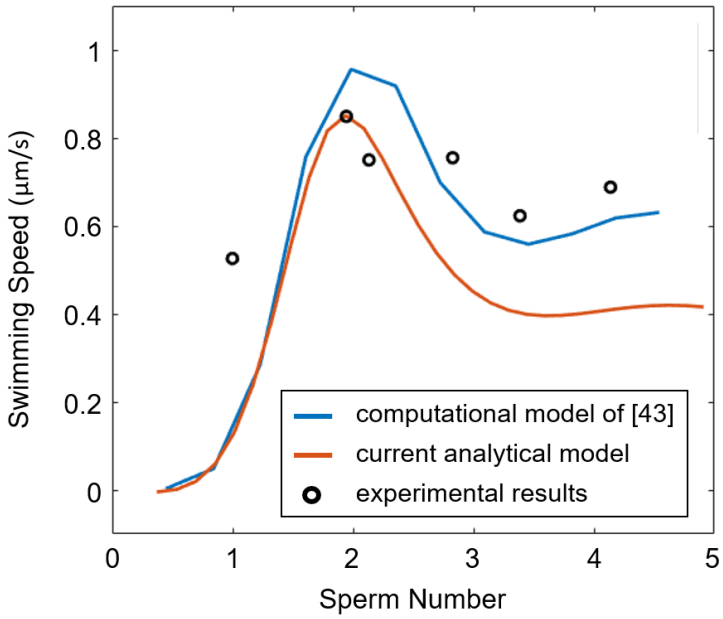

Figure 4.3: Swimming velocity vs. Sperm number for the swimmer prototype of Chapter 3. Solution of our current elasto-hydrodynamic model is overlaid onto experimental results and computational model predictions from our previously published study [43]. In experiments, Sperm number was varied by changing the tail length.

4.4 Design strategies: muscle contraction dynamics, drag, and actuation amplitude

The results show in Fig. 4.3 validate our elasto-hydrodynamic model. While the model under-predicts swimming speeds for higher values of Sp, its predictions of swimming speed for the optimum value of Sp match closely with experimental results and the predictions of previous computational models. Hence, in this section, we will use our elasto-hydrodynamic model to evaluate the performance of our swimmer designs. Moreover, to derive potential design strategies, we will utilize a key insight provided by the analysis of the theory presented above: For a given actuation mode and amplitude, the Sperm number alone characterizes the performance of the swimmer tails. All the relevant physical parameters (*i.e.*, tail dimensions and elastic modulus, fluid viscosity, and actuation frequency) are absorbed into the Sperm number, and the experimental data collapses onto a single curve (Fig 4.3). Data collapse was also demonstrated previously for a wide range of experimental conditions in a study by Yu *et al.* [85]. This simplifies the task of optimizing the swimmer's tails: One simply needs to operate at the optimum Sperm number.

Based on equation 4.12, the Sperm number depends on the dimensions of the tail, its elastic modulus, drag coefficient (determined by fluid viscosity and tail geometry), and actuation frequency. In our experiments, fluid viscosity and tail elastic modulus are fixed material properties, and the cross-sectional dimensions of the tail are tightly constrained by fabrication processes. As we will discuss below, the choices for actuation frequency are also limited and the optimum actuation frequency is determined by muscle contraction dynamics. Altogether, this leaves the tail length as the most feasible tuning parameter to adjust the value of Sp. The strategy to optimize tail performance is therefore to determine material properties, tail cross-sectional dimensions, and optimum actuation frequency, then cut the tails to the length that corresponds to the optimum value of the Sperm number (in our case, $Sp_{optimum} \cong 2$).

To determine the optimum actuation frequency, we must consider muscle contraction dynamics: Briefly, when a skeletal muscle fiber is stimulated, whether by a motor neuron or by an external electrical or optical pulse (for optogenetic muscle cells), an action potential is generated in the muscle fiber. As the action potential propagates, calcium ions are released from the sarcoplasmic reticulum, which in turn activate the actin-myosin apparatus, leading to contraction. As the calcium ions are transported back into the sarcoplasmic reticulum, the muscle cell relaxes back to baseline [26], [86]–[90]. The rise and relaxation times are determined by various intrinsic factors such as the calcium handling properties of the cell, and the myosin isoforms present [26].

Hence, for a given muscle fiber at a given time, the temporal shape of the force-time curve for a single twitch is fixed (amplitude can still be varied). Consequently, stimulating the muscle at increasing frequencies does not reduce the rise and relaxation times, but rather leads to accumulation of tension, giving rise to the characteristic force-frequency relationship (Fig. 4.4A).

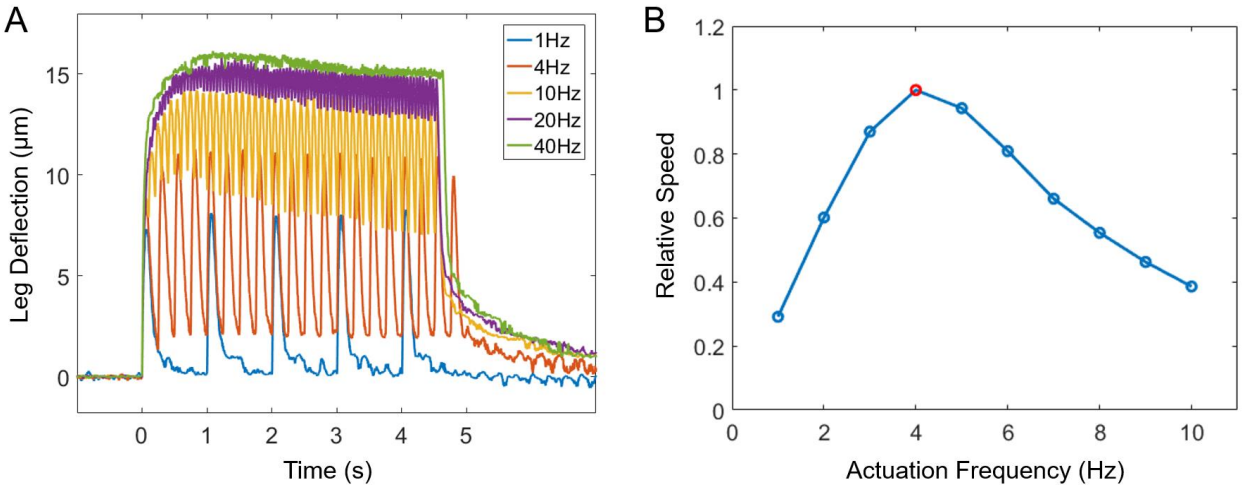

Figure 4.4. Determination of optimum actuation frequency based on muscle contraction dynamics. (A) Leg deflections of the swimmer scaffold due to muscle contractions at different stimulation frequencies. (B) Corresponding swimming speeds normalized by the maximum speed.

This force-frequency relationship (Fig. 4.4A) determines the optimum actuation frequency: At low frequencies, there are periods of time between two consecutive twitches when the muscle is at rest, the swimmer's body is not undergoing deformation, and no thrust is generated. As the stimulation frequency increases, the duty cycle, and therefore the swimming speed, increase. At the optimum frequency (~4Hz for our tissue engineered muscle strips), muscles are continuously generating deformation, and the bioactuator is operating at 100% duty cycle. If the stimulation frequency is increased further, summation is induced, where the muscle is not given enough time to relax fully before the next contraction. As a result, the total tension increases but the peak-to-peak amplitude of contraction force decreases, leading to suboptimal swimming speed (Fig. 4.4B).

Once the swimmer tail is operating at the optimum Sperm number, further modifications of the variables that are included in the Sperm number will not yield improvements in swimming performance. For further improvement, two possible strategies are to reduce drag on the swimmer body (head, legs, and tissues – viscous drag on the tails is already considered in the tail optimization scheme), and to increase the amplitude of actuation.

To investigate the possible effects of drag reduction, we solve our elasto-hydrodynamic model for different values of the equivalent body size, R_{body} in equation 4.8. As expected, our model predictions show that reducing the size of the swimmer body, thereby reducing viscous drag, leads to higher swimming speed. However, the improvement is not substantial. Reducing the body size by half provides approximately 1.5-fold increase in swimming speed. In the extreme case of zero body drag, swimming speed increases by a factor of 6.5 (Fig. 4.5A). Note, however, that this is not possible in practice because it requires $R_{body} = 0$, whereas the swimmer body, including the muscle tissue itself, will have a finite size.

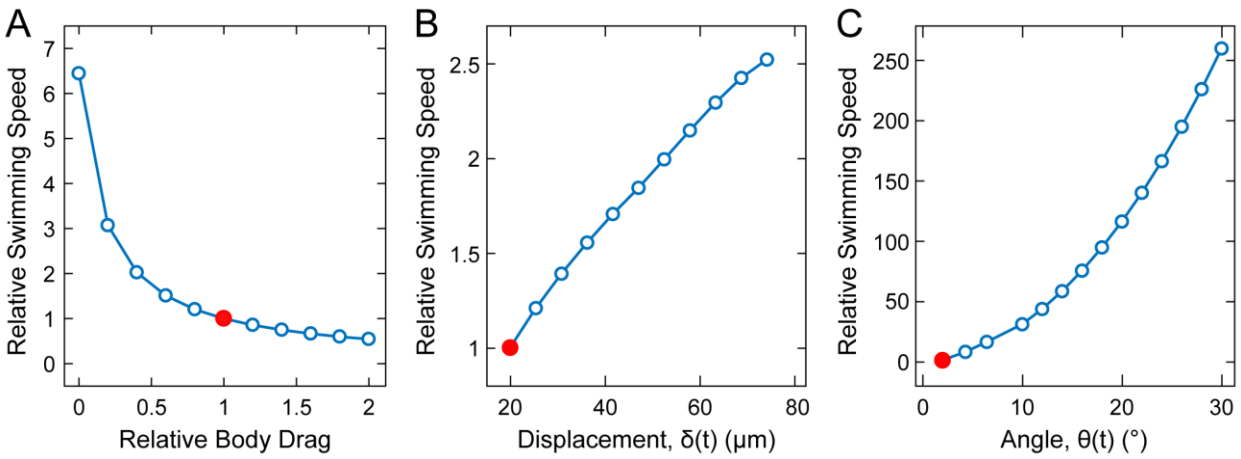

Figure 4.5: Model predictions for the effectiveness of potential design strategies. Relative swimming speed plotted against (A) relative body drag, and the (B) translational and (C) rotational amplitudes of actuation. The values of swimming speed and body drag are normalized by those of the swimmer prototype of Chapter 3, the results of which are shown by the red circles.

Next, we investigate the effects of increasing actuation amplitude. Actuation at the base of the tail can be decomposed into translation, with amplitude $\delta(t)$, and rotation, with amplitude $\theta(t)$ (Fig. 4.1). In the swimmer prototype of Chapter 3, bending of the legs due to muscle contractions produced $\delta \cong 20\ \mu m$ and $\theta \cong 1.5°$. In our simulations, we can independently vary the amplitudes of these two variables to examine their effect on swimming speed. Model predictions show that increasing δ does not lead to significant improvement in swimming speed (Fig. 4.5B). It is also difficult to increase δ in practice since it directly corresponds to the change in muscle length during contraction, which is limited. However, our model predicts that increasing θ can produce significant (up to two orders of magnitude) improvement in swimming speed (Fig. 4.5C). We therefore focus our efforts to redesign the swimmer on achieving high angular actuation amplitude.

4.5 Revised swimmer design

In our swimmer design, rotations at the base of the tail are provided by the rotations of the tip of the leg as it bends due to muscle contraction forces. For the initial swimmer prototype of chapter 3, the distance between the center of the muscle and the base of the leg (*i.e.*, the effective length of the leg) was approximately 500 μm, whereas the transverse deflection of the tip of the leg was approximately 20 μm (see Fig. 3.3), therefore generating relatively small rotation (1.5°). Increasing the angle of rotation of the tip of a bending beam can be achieved by increasing the magnitude of the transverse deflection (bending the beam more) or by reducing the length of the beam. The magnitude of transverse deflection is directly related to the shortening of the muscle as it contracts. In our experiments with tissue engineered muscles, both on the co-culture platform of chapter 2 and on the swimmer scaffold of chapter 3, the maximum deflections generated by the muscle strips were 20 to 25 μm, corresponding to a change in muscle length of ~10%. Since the magnitude of shortening of a muscle is limited by its anatomy, we do not expect to achieve significantly higher deflections. We therefore chose to redesign our swimmer scaffold to reduce the length of the legs.

Since the expected magnitude of transverse deflection is limited to 20-25 μm, achieving large angular rotations of the tip of the leg requires the length of the leg to be comparable to the magnitude of deflection. This presents a challenge because in our current design, the width of the muscle strip at the region where it wraps around the leg is ~200 μm. If we simply scale-down our initial prototype, reducing the effective length of the leg from 500 μm to 50 μm, for instance, then the width of the muscle strip would have to be scaled down to ~20 μm, which is approximately the diameter of a single myotube. Creating a single myotube wrapping around two compliant beams may not be practically feasible with our current tissue engineering methods. Furthermore, how much force and deflection such a construct would generate is unknown. To address this challenge, we chose to keep the dimensions of the muscle strip unchanged, but instead redesign the way it interfaces with the swimmer scaffold. Our revised design is illustrated below (Fig. 4.6A). Here, the muscle strips are bridging two grips which have numerous hook-shaped structures to facilitate anchorage. At their distal ends, the grips taper into a very thin (~10 μm-wide) connecting beam which transmits the muscle forces onto the tip of a short leg (Fig. 4.6B-C), which effectively acts as a compliant hinge.

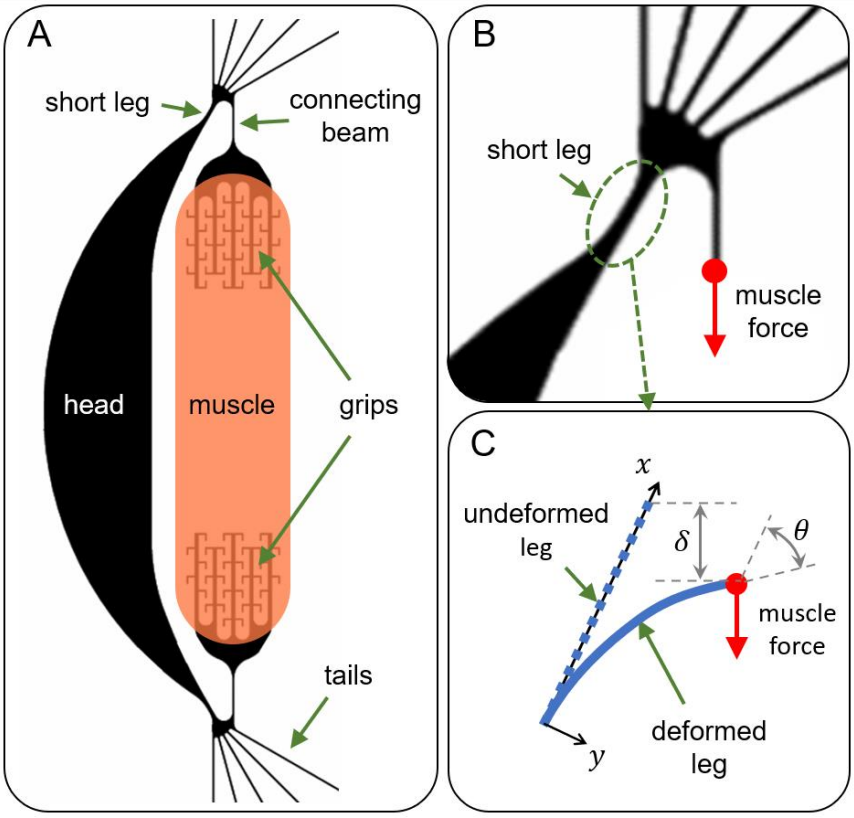

Figure 4.6: Revised swimmer design. (A) Schematic of the revised prototype showing a small head, which reduces drag, and two grips to anchor the muscle and transmit the contraction force onto the tips of short legs. (B) Zoomed-in view showing one of the short legs, and (C) the corresponding schematic illustrating the targeted large angle deformation.

We have proceeded to fabricate the revised swimmer prototype and test tissue seeding, using the methods described in chapter 3 for the previous swimmer prototype. The swimmer scaffold and temporary tissue seeding molds were fabricated by casting PDMS in microfabricated silicon molds. The scaffold was then sandwiched between the two temporary tissue seeding molds, creating a cavity around the two grips. This cavity is seeded with a suspension of C2C12 myoblasts in an ECM solution of type I collagen (2 mg/ml) and Matrigel (1 mg/ml) (Fig. 4.7A). After the ECM solution polymerizes, the cell-laden ECM gel compacts and forms a muscle strip anchored by the two grips (Fig. 4.7B). The temporary tissue seeding molds are then removed, and the grips which were rigidly anchored to the head are released (Fig. 4.7C).

In the previous swimmer prototype of chapter 3 and the co-culture platform of chapter 2, the muscle strips were wrapping around cantilever legs and T-shaped pillars, respectively. Anchorage was provided by macroscale mechanical encapsulation of the scaffold structure by the

tissue. In the revised design, however, anchorage relies on microscale encapsulation of the small hook-shaped structures on the grips, as well as the adhesion of cells and ECM to the PDMS scaffold. To promote the latter form of attachment, we coated the swimmer scaffolds with fibronectin by incubating in a 10 μg/ml fibronectin solution prior to assembling with the tissue seeding molds. The tissue seeding molds, on the other hand, were coated separately with 1% w/v Pluronic F127 to minimize cell and ECM attachment [91]. This allows the cell-laden ECM gel to detach from the surfaces of the tissue seeding molds and compact freely. We have confirmed that the muscle strips formed by this method do not slip off, and remain anchored to the grips long term (at least 2 weeks) in culture.

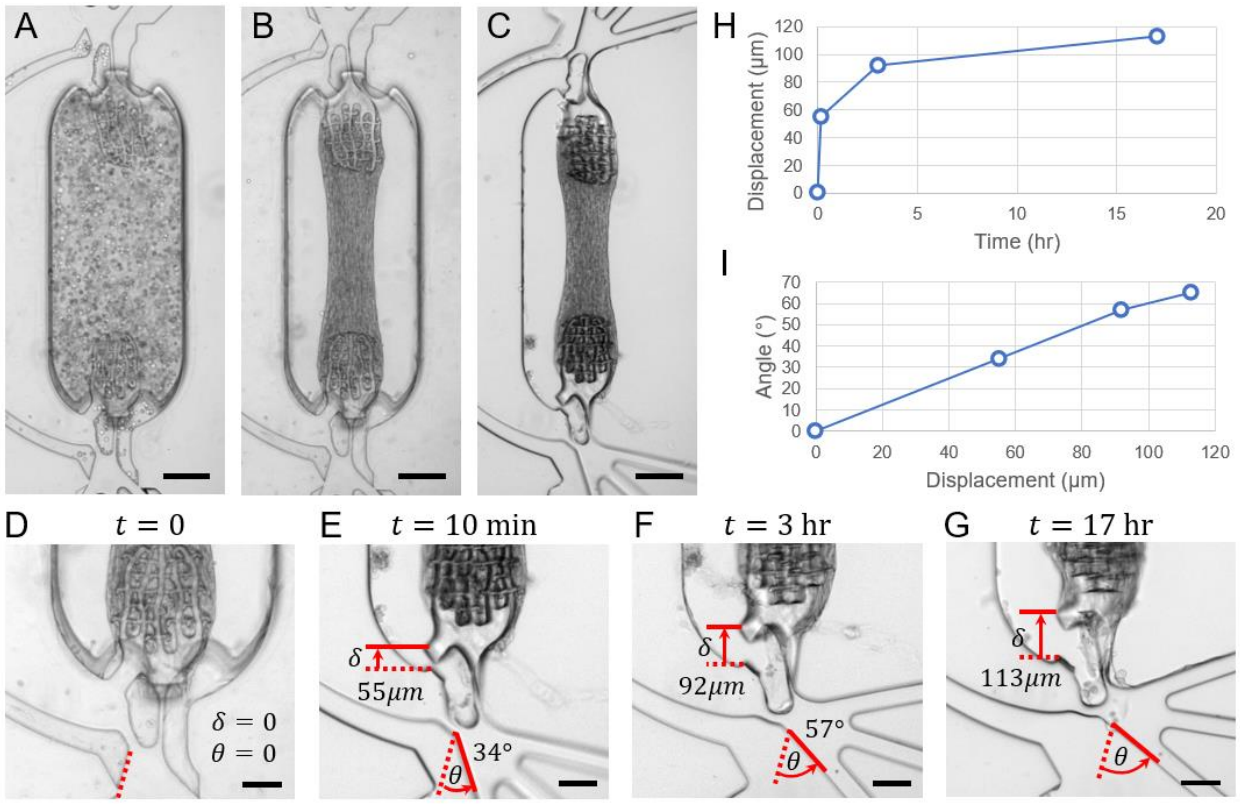

Figure 4.7: Experimental characterization of the leg deformations of the revised prototype under passive tension. (A-C) Muscle strip formation and release. Brightfield images showing (A) the swimmer scaffold immediately after seeding cell-ECM mixture, (B) muscle strip formed by compaction of the cell-laden ECM, and (C) the swimmer scaffold shortly after removing the temporary tissue seeding molds and releasing the grips from the head. Scale bars: 200 μm. (D-G) Deflections generated by passive tension. Brigtfield images taken (D) before, (E) 10 minutes after, (F) 3 hours after, and (G) 17 hours after releasing the grips from the head. Scale bars: 100 μm. (H) Grip displacement vs. time. (I) Rotation of the tip of the leg vs. grip displacement.

We characterized the deformations of the short leg under the passive tension of the muscle strip. The swimmer scaffolds are fabricated such that the grips are rigidly anchored to the head (Fig. 4.7D). This helps prevent deformations of the grips during handling, and ensures that the grips remain centered inside the cavity formed by the tissue seeding molds. Incidentally, it also allows the muscle strips to build up passive tension, and facilitates myoblast alignment during compaction. Once the tissues are compacted, the grips are released by manually cutting the beam anchoring them to the head. This directs the passive tension generated by the tissue towards the tip of the short and compliant legs, thereby generating leg deformations (Fig. 4.7E-G).

When the grips are released, the built-up passive tension results in a rapid increase in leg deflection within the first few hours. Deflection magnitude eventually reaches a plateau within 1 day (Fig. 4.7H). The corresponding angular rotation is approximately linearly proportional to the deflection, with a slope of ~0.6°/μm (Fig. 4.7I). For the swimmer prototype of chapter 3, the corresponding rotation-deflection relationship was ~0.075°/μm. Our revised swimmer design therefore achieves the aim of generating significantly higher angular actuation amplitudes. Since the dimensions of the muscle strips are similar to those of chapters 2 and 3, and the cell type and culture conditions remain unchanged, we expect the muscle strips on the revised swimmer scaffold to generate maximum deflections within the 20-25 μm range that were observed in our previous experiments. Based on the characterization of the leg deformation kinematics presented above (~0.6°/μm), deflections of this magnitude will lead to 12-15° rotations of the tips of the legs. In turn, according to the predictions of our elasto-hydrodynamic model, angular actuation magnitudes within this range will result in ~45 to ~70-fold improvement in swimming speed (Fig. 4.5C).

Lastly, we present a modification of the revised swimmer scaffold which accommodates neurons on the swimmer's head, enabling the utilization of neuromuscular units. The modified design consists of an extended head with an array of through-holes (Fig. 4.8A). The tissue seeding molds were also modified to include an additional cavity around the part of the perforated head. Once muscle strips bridging the two grips are formed as before, we seed the second cavity around the head with a neural cell-ECM mixture. Optogenetic stem cell-derived neurospheres containing motor neurons were obtained using the cell culture and differentiation methods that were described in chapters 2 and 3. However, instead of using the intact neurospheres directly, as was done in the previous chapters, here, we enzymatically dissociate them to obtain a single-cell suspension. The cells are then mixed with the ECM solution and seeded on the swimmer scaffold. This method

enables compartmentalized co-culture directly on the swimmer scaffold where the motor neuron cell bodies are located around the perforated region of the head, with a 500 μm-wide space between the neurons and the muscle strip that is covered with ECM gel to allow neurite outgrowth towards the muscle. By having the neural cell-laden ECM conform to the shape of the head, instead of seeding a relatively bulky neurosphere, we expect this design choice to also help reduce drag.

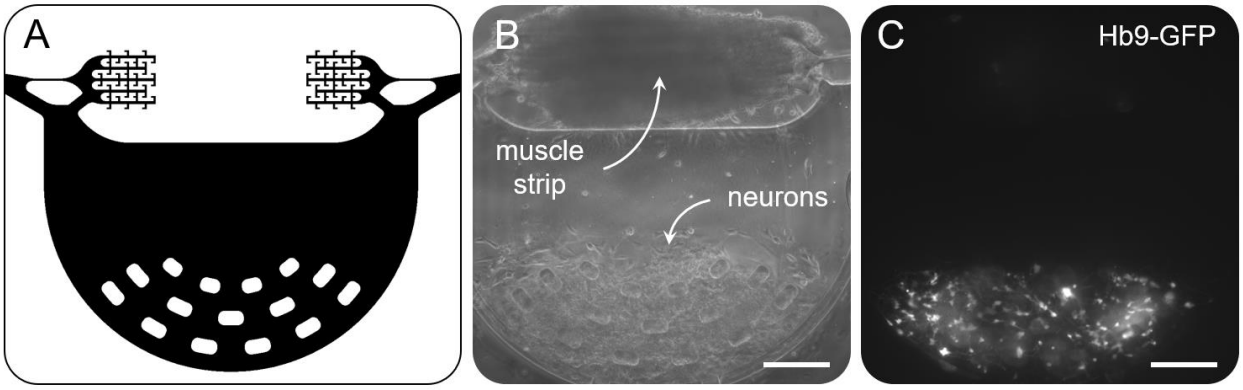

Figure 4.8: Revised swimmer design for neuromuscular bioactuator development. (A) Schematic of the modified design where the head is extended, and an array of through-holes are included to facilitate seeding neurons. (B) Brightfield and (C) fluorescence image of a co-culture sample showing Hb9-GFP^{+} motor neurons seeded around the perforated region of the head, approximately 500 μm away from the muscle strip, connected by a layer of ECM. Scale bars: 250 μm.

4.6 Summary and conclusions

We have developed an analytical model to evaluate potential design strategies to significantly improve the performance of our initial neuromuscular swimmer prototype. Our analysis revealed that the most effective way to improve swimming speed is to increase the angular amplitude of tail actuation. Guided by model predictions, we designed a novel swimmer prototype and developed the appropriate tissue culture techniques. Muscle strips were successfully formed on the new scaffold design, anchored by two grips that transmit the muscle force precisely onto short legs. We characterized the leg deformations to confirm that the revised prototype can generate sufficiently large angular actuation amplitudes. Based on the previous performance of our tissue engineered muscles, the new design is expected to achieve up to ~70-fold increase in swimming speed. We concluded with a further revision of our new swimmer design to achieve compartmentalized neuron-muscle co-culture on the swimmer scaffold.

CHAPTER 5: DISCUSSION AND OUTLOOK

5.1 Current state of the art

Development of biohybrid machines is rapidly expanding into new frontiers, and encouraging a continuing convergence between several disciplines including biology, engineering, education, and ethics [92]–[95].

Regarding neuromuscular actuation, apart from and concurrently with the work presented in this dissertation, there have been two studies published which demonstrated the development of neuromuscular units on free-standing scaffolds, with the aim to power the untethered locomotion of a biohybrid machine. While both studies provided evidence of muscle activity induced by neuronal stimulation, the evoked contractions were local, and did not have sufficient magnitude to power locomotion [39], [41]. The key distinction was that these studies were focused on biohybrid machines with sizes of ~1 cm, whereas the neuromuscular actuators we have demonstrated here are in the sub-millimeter size scale. In our case, the goal of operating in a low Reynolds number flow regime has naturally led us to develop miniature systems, containing several hundred neurons and a similar number of myotubes. This miniaturization increases the likelihood that most of the muscle fibers will be innervated successfully, allowing neuronal stimulation to evoke global contractions with sufficient magnitude. Scaling up, however, remains a challenge.

In terms of design and modeling, there have been several trends and novel advances. Many studies on the development of biohybrid machines (including our work) have demonstrated biomimetic scaffold designs, mimicking jellyfish [17], stingray [18], or spermatozoa [16], [43]. Borrowing from nature in this manner is an effective strategy for designing bioactuators, especially when the mechanics of locomotion of the organism that is being imitated is well-understood. This allows the designer to capitalize on existing theories and models. The work we have presented in chapter 4 of this dissertation is a good example, since the elasto-hydrodynamic model that we have developed to guide our design process was based on several decades of literature on the theory of flagellar locomotion. Conversely, biomimetic designs may also serve as experimental testbeds to study the biomechanics of the organism or system that is being imitated. They may also help elucidate design principles which could in turn be applied to conventional robotics [2].

Furthermore, it is possible to go beyond biomimetics and develop entirely novel systems using algorithmic design processes. This was demonstrated in a recent study where an evolutionary algorithm was used to generate, evaluate, and select novel cardiomyocyte powered bioactuator designs that achieved desired locomotor performance [96].

Once a conceptual blueprint for a bioactuator is proposed, whether it is inspired by biomimicry, algorithmic processes, or physical intuition, the next step is to implement it successfully. This is where modeling can be instrumental, by guiding the design of initial prototypes and optimizing their performance. Compliant systems undergoing large and nonlinear deformations are often difficult to model. Introducing active biological components such as muscle cells complicates the task even further. However, recent advances have produced computational simulation environments that can achieve this modeling task effectively [97]. These computational tools have been validated against benchmark problems [98] and have been used to model the dynamics of musculoskeletal systems [99]. Consequently, they have been utilized to assist the design of biohybrid machines [22], [43], [100].

As more novel biohybrid machines are being developed, assisted by advances in cell and tissue culture techniques and computational modeling tools, the question of how they may be used in real-world applications becomes more pressing. Current biohybrid systems powered by mammalian cells require carefully controlled environmental conditions (*e.g.*, temperature, pH, and osmolarity) to maintain their viability and function. This makes the deployment of biohybrid machines outside of a tissue culture lab especially challenging. However, there have been recent advances which aim to address this challenge. A recent study has demonstrated that skeletal muscle bioactuators can be cryopreserved for long term storage and transport, and that they maintain their functionality after revival [101]. Another study has demonstrated a method of encapsulating skeletal muscle bioactuators in collagen which allows them to operate in air [102]. While these technologies can potentially enable the utilization of biohybrid machines in the real-world, ensuring that the biohybrid machines achieve the desired functions once they are deployed outside of the lab is another matter. Remote control, for example by wireless electronics, is one option. Another, more exciting possibility (and the long-term ambition that the work presented in this dissertation is intended to serve) is the development of biohybrid machines that navigate their environment autonomously through neuronal circuits which perform sensing, process information, and coordinate motor activity.

5.2 Neural circuits for sensing, motor coordination, memory, and learning

The ability to command muscle activity through motor neurons in a bioactuator paves the way for further integration of neural circuits in biohybrid systems. Advances in stem cell biology have enabled directed differentiation of pluripotent stem cells into neurons of spinal cord identity [103], cortical neurons [104], and more recently, peripheral sensory neurons [105], thereby providing cell sources to possibly enhance the functionalities of *in vitro* neural networks. However, utilizing these cell sources to build neural circuits capable of sensing, motor coordination, information processing, and memory has so far not been demonstrated. To build such systems, having access to the essential building blocks is by no means sufficient. What is currently needed is an understanding of how different neuronal cells can be brought together to form functional units, and how they interact with each other as well as with muscles and the compliant scaffolds. The bioactuator platforms that are presented in this dissertation could serve as testbeds to help answer these questions.

As we have demonstrated in chapter 3, the neurons within our stem cell-derived neurospheres spontaneously form neural networks which produce synchronous and periodic bursting patterns (see Fig. 2.7E). The neurospheres we have used in these experiments were obtained by a directed differentiation protocol which produces neurons of spinal cord identity [63], [103]. Incidentally, in vertebrates, the spinal cord contains distinct neural circuits called central pattern generators (CPGs) which produce periodic bursting patterns to modulate muscle activity during locomotion [26]–[28]. While our neurospheres may emulate a single CPG, complex locomotion requires inter-segmental coordination of multiple CPGs. For example, the locomotor circuits of the lamprey generate the undulatory body deformations necessary for swimming by sequential activation of CPGs along the length of the spinal cord, each of which controls the activity of a separate muscle group [106]. Our neuromuscular bioactuator platform of chapter 2 is well-suited to investigate how *in vitro* locomotor networks may be built. The platform architecture can easily be modified to include a linear array of neural compartments, each seeded with a neurosphere innervating separate target muscle strips. Such a platform could be used to study potential methods of interfacing adjacent neurospheres such that they produce sequential activity propagating along the chain of neural compartments.

Another intriguing possibility is to use our neuromuscular bioactuator platforms to study memory and learning in *in vitro* neural networks. While memory is often used colloquially to refer

to explicit forms of memory (*e.g.*, remembering a phone number), which are attributes of the brain, neural networks in the spinal cord exhibit "implicit" forms of memory and learning such as habituation, sensitization, and reflex conditioning [26]. In our study of the neuromuscular swimmer of chapter 3, we had observed that repetitive stimulation of the neurons leads to a short-term attenuation of muscle activity and the corresponding swimming performance, both of which were recovered after rest (Fig. 3.4). As potential explanations, we had suggested muscle fatigue or neurotransmitter depletion at the NMJ. However, our results are also consistent with the hypothesis that our neural network was undergoing short-term habituation. For instance, in the classical example of the habituation of gill-withdrawal reflex in *aplysia californica*, repetitive stimulation leads to a decrease in synaptic vesicle release by excitatory neurons. The resulting attenuation in motor neuron output is recovered over time if repetitive stimulation is ceased [26], similar to our observation of recovery in the biohybrid swimmer.

However, further investigations are currently needed to reach a definitive conclusion regarding the hypothesis of short-term habituation. The experiment could be repeated with the addition of external electrical stimulation before and after repetitive neural stimulation. Electrical stimulation bypasses the NMJ and evokes muscle contractions directly. If electrical stimulation evokes contractions with similar amplitudes before and after neural stimulation, this will rule out muscle fatigue as an explanation. More direct evidence of neural involvement could be provided by experiments where neural activity is measured simultaneously with muscle activity. In our current setup, muscle force is quantified by optical measurement of pillar or leg deflections, but there is no direct readout of neural activity. The latter could be achieved by several means including calcium imaging or by fabricating scaffolds with embedded electrodes for electrophysiological measurement. Further evidence of the precise mechanism of action may also be obtained by genetic knockout studies.

Another interesting avenue of investigation is the possibility of *in vitro* neural networks to exhibit sensitization to repetitive stimuli. *In vivo*, the distinction often involves physiological differences in the circuits. For instance, in the *aplysia* gill-withdrawal reflex, habituation and sensitization involve, respectively, a decrease in glutamate vesicle release and an increase in serotonin vesicle release by separate excitatory interneurons [26]. In our experiments, by modifying the stem cell differentiation protocol to yield neural clusters with different physiological content (*e.g.*, clusters containing different numbers of serotonergic vs. glutamatergic neurons), it

may be possible to tune which mode of implicit memory (habituation or sensitization) is exhibited by the neural networks.

Furthermore, the distinction *in vivo* between habituation and sensitization can also be interpreted within the broader context of the animal's behavior: Repetitive stimuli that are neither beneficial nor harmful tend to lead to habituation (the animal learns to ignore the stimulus) whereas harmful stimuli lead to sensitization (the animal learns to fear the stimulus). For neural networks that are developed *in vitro*, such a behavioral interpretive framework is currently not available. Our bioactuator platforms could potentially serve as testbeds to help classify different system responses and different types of stimuli (*e.g.*, optical, electrical, tactile, pharmacological) in a behavioral context for biohybrid machines.

REFERENCES

[1] R. D. Kamm *et al.*, "Perspective: The promise of multi-cellular engineered living systems," *APL Bioeng.*, vol. 2, no. 4, p. 040901, 2018.

[2] R. Pfeifer, M. Lungarella, and F. Iida, "Self-Organization, Embodiment, and Biologically Inspired Robotics," *Science (80-.).*, vol. 318, no. 5853, pp. 1088–1093, 2007.

[3] V. A. Webster-Wood, O. Akkus, U. A. Gurkan, H. J. Chiel, and R. D. Quinn, "Organismal engineering: Toward a robotic taxonomic key for devices using organic materials," *Sci. Robot.*, vol. 2, no. 12, pp. 1–19, 2017.

[4] C. Zhang, W. Wang, N. Xi, Y. Wang, and L. Liu, "Development and Future Challenges of Bio-Syncretic Robots," *Engineering*, vol. 4, no. 4, pp. 452–463, 2018.

[5] R. M. Duffy and A. W. Feinberg, "Engineered skeletal muscle tissue for soft robotics: Fabrication strategies, current applications, and future challenges," *Wiley Interdiscip. Rev. Nanomedicine Nanobiotechnology*, vol. 6, no. 2, pp. 178–195, 2014.

[6] S. Ostrovidov *et al.*, "Skeletal muscle tissue engineering: Methods to form skeletal myotubes and their applications," *Tissue Eng. - Part B Rev.*, vol. 20, no. 5, pp. 403–436, 2014.

[7] A. Khodabukus and K. Baar, "Factors that affect tissue-engineered skeletal muscle function and physiology," *Cells Tissues Organs*, vol. 202, no. 3–4. 2016.

[8] Y. Akiyama, S. Park, and S. Takayama, "Design Considerations for Muscle-Actuated Biohybrid Devices," in *Nanotechnology and Microfluidics*, 2020.

[9] L. Ricotti *et al.*, "Biohybrid actuators for robotics: A review of devices actuated by living cells," *Sci. Robot.*, vol. 2, no. 12, pp. 1–18, 2017.

[10] V. Chan, H. H. Asada, and R. Bashir, "Utilization and control of bioactuators across multiple length scales," *Lab Chip*, vol. 14, no. 4, pp. 653–670, 2014.

[11] T. Patino, R. Mestre, and S. Sánchez, "Miniaturized soft bio-hybrid robotics: A step forward into healthcare applications," *Lab Chip*, vol. 16, no. 19, pp. 3626–3630, 2016.

[12] A. W. Feinberg, "Biological Soft Robotics," *Annu. Rev. Biomed. Eng.*, vol. 17, no. 1, pp. 243–265, 2015.

[13] Y. Morimoto, H. Onoe, and S. Takeuchi, "Biohybrid robot powered by an antagonistic pair of skeletal muscle tissues," *Sci. Robot.*, vol. 3, no. 18, 2018.

[14] Y. Tanaka, K. Sato, T. Shimizu, M. Yamato, T. Okano, and T. Kitamori, "A micro-spherical heart pump powered by cultured cardiomyocytes," *Lab Chip*, vol. 7, no. 2, pp. 207–212, 2007.

[15] Z. Li *et al.*, "Biohybrid valveless pump-bot powered by engineered skeletal muscle," *Proc. Natl. Acad. Sci. U. S. A.*, vol. 116, no. 5, 2019.

[16] B. J. Williams, S. V. Anand, J. Rajagopalan, and M. T. A. Saif, "A self-propelled biohybrid swimmer at low Reynolds number," *Nat. Commun.*, vol. 5, pp. 1–8, 2014.

[17] J. C. Nawroth *et al.*, "A tissue-engineered jellyfish with biomimetic propulsion," *Nat. Biotechnol.*, vol. 30, no. 8, pp. 792–797, 2012.

[18] S.-J. Park *et al.*, “Phototactic guidance of a tissue-engineered soft-robotic ray,” *Science (80-.).*, vol. 353, no. 6295, pp. 158–162, 2016.

[19] A. W. Feinberg, S. Sheehy, K. K. Parker, A. Feigel, S. S. Shevkoplyas, and G. M. Whitesides, “Muscular thin films for building actuators and powering devices,” *Science (80-.).*, vol. 317, no. 5843, pp. 1366–1370, 2007.

[20] V. Chan, K. Park, M. B. Collens, H. Kong, T. A. Saif, and R. Bashir, “Development of miniaturized walking biological machines,” *Sci. Rep.*, vol. 2, 2012.

[21] C. Cvetkovic *et al.*, “Three-dimensionally printed biological machines powered by skeletal muscle,” *Proc. Natl. Acad. Sci.*, vol. 111, no. 28, pp. 10125–10130, 2014.

[22] G. J. Pagan-Diaz *et al.*, “Simulation and Fabrication of Stronger, Larger, and Faster Walking Biohybrid Machines,” *Adv. Funct. Mater.*, vol. 28, no. 23, pp. 1–13, 2018.

[23] R. Raman *et al.*, “Optogenetic skeletal muscle-powered adaptive biological machines,” *Proc. Natl. Acad. Sci.*, vol. 113, no. 13, pp. 3497–3502, 2016.

[24] R. Raman *et al.*, “Damage, Healing, and Remodeling in Optogenetic Skeletal Muscle Bioactuators,” *Adv. Healthc. Mater.*, vol. 6, no. 12, 2017.

[25] C. Cvetkovic *et al.*, “Investigating the Life Expectancy and Proteolytic Degradation of Engineered Skeletal Muscle Biological Machines,” *Sci. Rep.*, 2017.

[26] E. R. Kandel, J. H. Schwartz, T. M. Jessell, S. A. Siegelbaum, and A. J. Hudspeth, *Principles of neural science*, 5th ed. McGraw-Hill Medical, 2013.

[27] S. Grillner, “The motor infrastructure: From ion channels to neuronal networks,” *Nat. Rev. Neurosci.*, vol. 4, no. 7, pp. 573–586, 2003.

[28] S. Grillner, “Biological Pattern Generation: The Cellular and Computational Logic of Networks in Motion,” *Neuron*, vol. 52, no. 5, pp. 751–766, 2006.

[29] M. C. Tresch and O. Kiehn, “Motor coordination without action potentials in the mammalian spinal cord.,” *Nat. Neurosci.*, vol. 3, no. 6, pp. 593–599, 2000.

[30] Z. W. Hall and J. R. Sanes, “Synaptic structure and development: The neuromuscular junction,” *Cell*, vol. 72, pp. 99–121, 1993.

[31] J. R. Sanes and J. W. Lichtman, “Development of the vertebrate neuromuscular junction,” *Annu. Rev. Neurosci.*, vol. 22, pp. 389–442, 1999.

[32] H. Wu, W. C. Xiong, and L. Mei, “To build a synapse: signaling pathways in neuromuscular junction assembly,” *Development*, vol. 137, no. 7, pp. 1017–1033, 2010.

[33] M. Knipper and R. J. Rylett, “A new twist in an old story: the role for crosstalk of neuronal and trophic activity,” *Neurochem. Int.*, vol. 31, no. 5, pp. 659–676, 1997.

[34] N. Tabti and M. Poo, “Spontaneous synaptic activity at developing neuromuscular junctions.,” *Prog. Brain Res.*, vol. 84, pp. 63–72, 1990.

[35] O. E. Harish and M. Poo, “Retrograde modulation at developing neuromuscular synapses: Involvement of G protein and arachidonic acid cascade,” *Neuron*, vol. 9, no. 6, pp. 1201–1209, 1992.

[36] M. A. Fox *et al.*, “Distinct Target-Derived Signals Organize Formation, Maturation, and

Maintenance of Motor Nerve Terminals," *Cell*, vol. 129, pp. 179–193, 2007.

[37] Y. Morimoto, M. Kato-Negishi, H. Onoe, and S. Takeuchi, "Three-dimensional neuron-muscle constructs with neuromuscular junctions," *Biomaterials*, vol. 34, no. 37, pp. 9413–9419, 2013.

[38] S. G. M. Uzel *et al.*, "Microfluidic device for the formation of optically excitable, three-dimensional, compartmentalized motor units," *Sci. Adv.*, vol. 2, no. 8, p. e1501429, 2016.

[39] C. Cvetkovic, M. H. Rich, R. Raman, H. Kong, and R. Bashir, "A 3D-printed platform for modular neuromuscular motor units," *Microsystems Nanoeng.*, vol. 3, no. December 2016, p. 17015, 2017.

[40] T. Osaki, S. G. M. Uzel, and R. D. Kamm, "On-chip 3D neuromuscular model for drug screening and precision medicine in neuromuscular disease," *Nat. Protoc.*, 2020.

[41] C. D. Kaufman *et al.*, "Emergence of functional neuromuscular junctions in an engineered, multicellular spinal cord-muscle bioactuator," *APL Bioeng.*, vol. 4, no. 2, 2020.

[42] O. Aydin *et al.*, "Development of 3D neuromuscular bioactuators," *APL Bioeng.*, vol. 4, no. 1, 2020.

[43] O. Aydin *et al.*, "Neuromuscular actuation of biohybrid motile bots," *Proc. Natl. Acad. Sci.*, vol. 116, no. 40, pp. 19841–19847, 2019.

[44] Y. Morimoto, H. Onoe, and S. Takeuchi, "Biohybrid device with antagonistic skeletal muscle tissue for measurement of contractile force," *Adv. Robot.*, vol. 33, no. 5, pp. 208–218, 2019.

[45] Y. Shin *et al.*, "Microfluidic assay for simultaneous culture of multiple cell types on surfaces or within hydrogels," *Nat. Protoc.*, vol. 7, no. 7, pp. 1247–1259, 2012.

[46] C. E. Henderson, M. Huchet, and J.-P. Changeux, "Neurite outgrowth from embryonic chicken spinal neurons is promoted by media conditioned by muscle cells," *Proc Natl Acad Sci U S A*, vol. 78, no. 4, pp. 2625–2629, 1981.

[47] E. E. Zahavi, A. Ionescu, S. Gluska, T. Gradus, K. Ben-Yaakov, and E. Perlson, "A compartmentalized microfluidic neuromuscular co-culture system reveals spatial aspects of GDNF functions," *J. Cell Sci.*, vol. 128, no. 6, pp. 1241–1252, 2015.

[48] S. Chiron *et al.*, "Complex interactions between human myoblasts and the surrounding 3D fibrin-based matrix," *PLoS One*, vol. 7, no. 4, p. e36173, 2012.

[49] W. R. Legant, A. Pathak, M. T. Yang, V. S. Deshpande, R. M. McMeeking, and C. S. Chen, "Microfabricated tissue gauges to measure and manipulate forces from 3D microtissues," *Proc. Natl. Acad. Sci.*, vol. 106, no. 25, pp. 10097–10102, 2009.

[50] N. Rabieh, S. M. Ojovan, N. Shmoel, H. Erez, E. Maydan, and M. E. Spira, "On-chip, multisite extracellular and intracellular recordings from primary cultured skeletal myotubes," *Sci. Rep.*, vol. 6, no. November, pp. 1–15, 2016.

[51] E. Bandi *et al.*, "Autocrine activation of nicotinic acetylcholine receptors contributes to Ca2+ spikes in mouse myotubes during myogenesis," *J. Physiol.*, vol. 568, no. 1, pp. 171–180, 2005.

[52] S. Thesleff, “Different kinds of acetylcholine release from the motor nerve,” *Int. Rev. Neurobiol.*, vol. 28, pp. 59–88, 1986.

[53] S. Thesleff, “Functional aspects of quantal and non-quantal release of acetylcholine at the neuromuscular junction,” *Prog. Brain Res.*, vol. 84, no. C, pp. 93–99, 1990.

[54] Y. I. Kim, T. Lomo, M. T. Lupa, and S. Thesleff, “Miniature end-plate potentials in rat skeletal muscle poisoned with botulinum toxin,” *J Physiol*, vol. 356, pp. 587–599, 1984.

[55] Z.-P. Xie and M.-M. Poo, “Initial events in the formation of neuromuscular synapse: Rapid induction of acetylcholine release from embryonic neuron,” *Proc Natl Acad Sci U S A*, vol. 83, pp. 7069–7073, 1986.

[56] Y. Kidokoro and M. Saito, “Early cross-striation formation in twitching Xenopus myocytes in culture,” *Proc Natl Acad Sci U S A*, vol. 85, no. 6, pp. 1978–1982, 1988.

[57] M. Weitkunat, M. Brasse, A. R. Bausch, and F. Schnorrer, “Mechanical tension and spontaneous muscle twitching precede the formation of cross-striated muscle *in vivo*,” *Development*, vol. 144, no. 7, pp. 1261–1272, 2017.

[58] A. F. M. Johnstone, G. W. Gross, D. G. Weiss, O. H. U. Schroeder, A. Gramowski, and T. J. Shafer, “Microelectrode arrays: A physiologically based neurotoxicity testing platform for the 21st century,” *Neurotoxicology*, vol. 31, no. 4, pp. 331–350, 2010.

[59] E. Biffi, G. Regalia, A. Menegon, G. Ferrigno, and A. Pedrocchi, “The influence of neuronal density and maturation on network activity of hippocampal cell cultures: A methodological study,” *PLoS One*, vol. 8, no. 12, p. e83899, 2013.

[60] D. A. Wagenaar, J. Pine, and S. M. Potter, “An extremely rich repertoire of bursting patterns during the development of cortical cultures,” *BMC Neurosci.*, vol. 7, pp. 1–18, 2006.

[61] S. Illes, W. Fleischer, M. Siebler, H. P. Hartung, and M. Dihné, “Development and pharmacological modulation of embryonic stem cell-derived neuronal network activity,” *Exp. Neurol.*, vol. 207, no. 1, pp. 171–176, 2007.

[62] T. J. Heikkilä *et al.*, “Human embryonic stem cell-derived neuronal cells form spontaneously active neuronal networks in vitro,” *Exp. Neurol.*, vol. 218, pp. 109–116, 2009.

[63] H. Wichterle and M. Peljto, “Differentiation of mouse embryonic stem cells to spinal motor neurons,” *Curr. Protoc. Stem Cell Biol.*, no. SUPPL. 5, pp. 1–9, 2008.

[64] C. Brennen and H. Winet, “Fluid Mechanics of Propulsion by Cilia and Flagella,” *Annu. Rev. Fluid Mech.*, vol. 9, no. 1, pp. 339–398, 1977.

[65] J. J. Blum and M. Hines, “Biophysics of flagellar motility,” *Q. Rev. Biophys.*, vol. 12, no. 2, pp. 103–180, 1979.

[66] I. R. Gibbons, “Cilia and flagella of eukaryotes,” *J. Cell Biol.*, vol. 91, no. 3 II, pp. 107s-124s, 1981.

[67] E. Lauga, “Floppy swimming: Viscous locomotion of actuated elastica,” *Phys. Rev. E - Stat. Nonlinear, Soft Matter Phys.*, 2007.

[68] E. Lauga and T. R. Powers, “The hydrodynamics of swimming microorganisms,” *Reports*

Prog. Phys., vol. 72, no. 9, 2009.

[69] E. M. Purcell, "Life at low Reynolds number," *Am. J. Phys.*, vol. 45, pp. 3–11, 1977.

[70] N. J. De Mestre and W. B. Russel, "Low-Reynolds-number translation of a slender cylinder near a plane wall," *J. Eng. Math.*, vol. 9, no. 2, pp. 81–91, 1975.

[71] S. O. Rizzoli and W. J. Betz, "Synaptic vesicle pools," *Nature Reviews Neuroscience*. 2005.

[72] B. Reid, C. R. Slater, and G. S. Bewick, "Synaptic Vesicle Dynamics in Rat Fast and Slow Motor Nerve Terminals," *J. Neurosci.*, vol. 19, no. 7, pp. 2511–2521, 2018.

[73] W. J. Betz and G. S. Bewick, "Optical analysis of synaptic vesicle recycling at the frog neuromuscular junction," *Science (80-.).*, 1992.

[74] J. Rajagopalan and M. T. A. Saif, "Fabrication of freestanding 1-D PDMS microstructures using capillary micromolding," *J. Microelectromechanical Syst.*, vol. 22, no. 5, pp. 992–994, 2013.

[75] J. GRAY and G. J. HANCOCK, "The Propulsion of Sea-Urchin Spermatozoa," *J. Exp. Biol.*, vol. 32, no. 4, 1955.

[76] K. E. Machin, "Wave propagation along flagella," *J. Exp. Biol.*, vol. 35, no. 4, pp. 796–806, Dec. 1958.

[77] C. H. Wiggins, D. Riveline, A. Ott, and R. E. Goldstein, "Trapping and wiggling: Elastohydrodynamics of driven microfilaments," *Biophys. J.*, vol. 74, no. 2 I, pp. 1043–1060, 1998.

[78] C. H. Wiggins and R. E. Goldstein, "Flexive and propulsive dynamics of elastica at low reynolds number," *Phys. Rev. Lett.*, vol. 80, no. 17, 1998.

[79] R. G. Cox, "The motion of long slender bodies in a viscous fluid. Part 1. General theory," *J. Fluid Mech.*, vol. 44, no. 04, p. 791, 1970.

[80] D. Leith, "Drag on nonspherical objects," *Aerosol Sci. Technol.*, vol. 6, no. 2, 1987.

[81] C. P. Lowe, "Dynamics of filaments: Modelling the dynamics of driven microfilaments," *Philos. Trans. R. Soc. B Biol. Sci.*, vol. 358, no. 1437, pp. 1543–1550, 2003.

[82] M. C. Lagomarsino, F. Capuani, and C. P. Lowe, "A simulation study of the dynamics of a driven filament in an Aristotelian fluid," *J. Theor. Biol.*, vol. 224, no. 2, 2003.

[83] J. J. Abbott *et al.*, "How should microrobots swim?," in *International Journal of Robotics Research*, 2009, vol. 28, no. 11–12.

[84] R. Dreyfus, J. Baudry, M. L. Roper, M. Fermigier, H. A. Stone, and J. Bibette, "Microscopic artificial swimmers," *Nature*, vol. 437, no. 7060, pp. 862–865, 2005.

[85] T. S. Yu, E. Lauga, and A. E. Hosoi, "Experimental investigations of elastic tail propulsion at low Reynolds number," *Phys. Fluids*, 2006.

[86] A. F. Huxley and R. M. Simmons, "Proposed mechanism of force generation in striated muscle," *Nature*, vol. 233, no. 5321, 1971.

[87] S. Ebashi, M. Endo, and I. Ohtsuki, "Control of muscle contraction," *Q. Rev. Biophys.*,

vol. 2, no. 4, 1969.

[88] S. Ebashi, “Calcium ions and muscle contraction,” *Nature*, vol. 240, no. 5378. 1972.

[89] M. A. Geeves and K. C. Holmes, “Structural mechanism of muscle contraction,” *Annual Review of Biochemistry*, vol. 68. 1999.

[90] M. A. Geeves and K. C. Holmes, “The molecular mechanism of muscle contraction,” *Advances in Protein Chemistry*, vol. 71. 2005.

[91] K. Boxshall, M. H. Wu, Z. Cui, Z. Cui, J. F. Watts, and M. A. Baker, “Simple surface treatments to modify protein adsorption and cell attachment properties within a poly(dimethylsiloxane) micro-bioreactor,” in *Surface and Interface Analysis*, 2006, vol. 38, no. 4.

[92] L. Sun *et al.*, “Biohybrid robotics with living cell actuation,” *Chemical Society Reviews*, vol. 49, no. 12. 2020.

[93] A. Menciassi, S. Takeuchi, and R. D. Kamm, “Biohybrid systems: Borrowing from nature to make better machines,” *APL Bioengineering*, vol. 4, no. 2. 2020.

[94] R. Raman and R. Bashir, “Biomimicry, Biofabrication, and Biohybrid Systems: The Emergence and Evolution of Biological Design,” *Adv. Healthc. Mater.*, vol. 6, no. 20, 2017.

[95] M. Sample *et al.*, “Multi-cellular engineered living systems: building a community around responsible research on emergence,” *Biofabrication*, 2019.

[96] S. Kriegman, D. Blackiston, M. Levin, and J. Bongard, “A scalable pipeline for designing reconfigurable organisms,” *Proc. Natl. Acad. Sci. U. S. A.*, vol. 117, no. 4, 2020.

[97] N. Naughton, J. Sun, A. Tekinalp, T. Parthasarathy, G. Chowdhary, and M. Gazzola, “Elastica: A Compliant Mechanics Environment for Soft Robotic Control,” *IEEE Robot. Autom. Lett.*, vol. 6, no. 2, 2021.

[98] M. Gazzola, L. H. Dudte, A. G. McCormick, and L. Mahadevan, “Forward and inverse problems in the mechanics of soft filaments,” *R. Soc. Open Sci.*, vol. 5, no. 6, 2018.

[99] X. Zhang, F. K. Chan, T. Parthasarathy, and M. Gazzola, “Modeling and simulation of complex dynamic musculoskeletal architectures,” *Nat. Commun.*, vol. 10, no. 1, 2019.

[100] J. Wang *et al.*, “Computationally Assisted Design and Selection of Maneuverable Biological Walking Machines,” *Adv. Intell. Syst.*, vol. 3, no. 5, 2021.

[101] L. Grant *et al.*, “Long-Term Cryopreservation and Revival of Tissue-Engineered Skeletal Muscle,” *Tissue Eng. - Part A*, vol. 25, no. 13–14, 2019.

[102] Y. Morimoto, H. Onoe, and S. Takeuchi, “Biohybrid robot with skeletal muscle tissue covered with a collagen structure for moving in air,” *APL Bioeng.*, vol. 4, no. 2, 2020.

[103] H. Wichterle, I. Lieberam, J. A. Porter, and T. M. Jessell, “Wichterle-2002 Directed differentiation of embryonic stem cells into motor neurons.pdf,” vol. 110, pp. 385–397, 2002.

[104] M. Eiraku *et al.*, “Self-Organized Formation of Polarized Cortical Tissues from ESCs and Its Active Manipulation by Extrinsic Signals,” *Cell Stem Cell*, vol. 3, no. 5, pp. 519–532,

2008.

[105] M. Z. P. Guimarães *et al.*, “Generation of iPSC-Derived Human Peripheral Sensory Neurons Releasing Substance P Elicited by TRPV1 Agonists,” *Front. Mol. Neurosci.*, vol. 11, no. August, pp. 1–17, 2018.

[106] P. Wallén and T. L. Williams, “Fictive locomotion in the lamprey spinal cord in vitro compared with swimming in the intact and spinal animal.,” *J. Physiol.*, vol. 347, no. 1, 1984.